A multi-disciplinary design optimization framework with integrated structural transformation for highly loaded radial turbines

By Luca Martorelli

Delft University of Technology

TU Delft

A multi-disciplinary design optimization framework with integrated structural transformation for highly loaded radial turbines

by

Luca Martorelli

to obtain the degree of Master of Science
at the Delft University of Technology,
to be defended publicly on January 12th, 2023 at 9:00 AM.

Student number:	4936906	
Project duration:	September, 2021 – January, 2023	
Thesis committee:	Ir. M. (Matteo) Majer,	Daily Supervisor
	Dr. ir. M. (Matteo) Pini,	Responsible Supervisor
	Prof. dr. ir. P. (Piero) Colonna	
	Dr. ir. S.J. (Steven) Hulshoff	

TU Delft

Summary

During the last decades, the awareness towards environmental concerns has sharply strengthened, boosting research for a better exploitation of the limited resources available, particularly in the energy and transportation sectors. Therefore, many efforts are being made nowadays to obtain increasingly efficient turbomachinery components, keys in these fields.
In this context, the use of CFD-based optimizations is becoming a standard for turbomachinery design. Although their use can lead to great performance improvements of the machine, there are still a number of shortcomings in the common design procedure of turbomachines. In fact, when only considering the fluid dynamic behaviour of a part, many other important aspects might be neglected, such as the structural behaviour of the component. General practice in industry is to optimize the “loaded”, or “hot” design, hence the geometry that the component has during operation. Subsequently, the structural integrity of the component is checked to investigate the mechanical viability of the part. Only as a last step, what is called a *hot-to-cold transformation* is performed. This is a structural transformation used to retrieve the “unloaded”, or “cold”, geometry by subtracting the deformations the part undergoes while running. This is the shape the part has after manufacturing in order to achieve the desired ”hot” geometry. This typical design procedure has the disadvantage to only retrospectively check for structural viability and manufacturability of the part.
This thesis project aims at developing a multidisciplinary optimization method where the structural behaviour of the part can be checked already in the first part of the design process. This is done by using ”cold” design as first guess of the optimization, and by performing fluid-structure interaction simulations to predict the deformation of the part, and simultaneously simulate the behaviour of the flow field. This allows to apply constraints directly on the to-be-manufactured geometry, hence obtaining optimal impellers designs, while also considering manufacturing constraints. This multidisciplinary optimization can also provide valuable information to help on the trade-offs on materials and manufacturing methods to be used. As for this project, only the deformations of the part are considered. However, the framework can be easily extended to also investigate the stresses of the component, and hence its mechanical viability.
From the results obtained, an optimum design is found starting from the turbine ”cold” design, with an increase of efficiency of over 1%. Moreover, it has been observed that for this specific case the design satisfied the manufacturing constrains applied.
To conclude, one of the most important findings of this research has been the strong efficiency gap found between ”cold” and ”hot” design for the same design point. In fact, it has been observed that high deformations up to 0.461mm (compared to a blade with 0.4mm of tip thickness) and an efficiency gap up to a 0.79% difference were found in the design spaces investigated. This further corroborate the importance of a multidisciplinary approach for high loaded turbomachinery components.

Contents

List of Figures

List of Tables

Nomenclature

Abbreviations

Abbreviation	Definition
ANN	Artificial Neural Network
CFD	Computational Fluid Dynamic
CM	Control Mass
CNC	Computer Numerical Control
CV	Control Volume
DoE	Design of Experiments
DNS	Direct Numerical Simulations
ECM	Electrochemical Machining
EDM	Electro Discharge Machining
FEA	Finite Element Analysis
FEM	Finite Element Method
FSI	Fluid-Structure Interaction
LES	Large Eddy Simulations
LHS	Latin Hypercube Sampling
NLPQL	Nonlinear Programming by Quadratic Lagrangian
NS	Navier-Stokes
ORC	Organic Rankine Cycle
ORCHID	ORC Hybrid Integrated Device
OSF	Optimal Space Filling
RANS	Reynolds-Averaged Navier-Stokes
RIT	Radial Inlet Turbine
RS	Response Surface
RSO	Response Surface Optimization
SC	Study Case
SBO	Surrogate-Based Optimization
SLM	Selective Laser Melting
SM	Surrogate Model
SST	Shear Stress Transport

1

Introduction

During the last decades, the world witnessed a rise in fossil fuel cost, accompanied by an exploitation of not renewable resources and an increase of atmospheric pollution. This, together with a the steep rise of the population over the last 50 years, has led to the necessity of a further development of the energy and transportation sectors. As a consequence, the world observed a sharp strengthening of environmental awareness and a rapid evolution in these industries.
In this regard, turbomachines are of utmost importance. To make some examples, gas turbines are used for energy extraction, turbochargers for automotive applications, turbofan or turbojet engines and pump fed rocket engines for aviation and space propulsion respectively, just to mention a few. Therefore, increasing the efficiency of turbomachinery components has become one of the main engineering focuses in order to benefit the most out of the limited resources available. Moreover, the strong developments in the field of Computational Fluid Dynamics (CFD) seen in recent years, resulted in the spread of CFD-based optimizations for the design of such components [1][2][3], as well as in many other fields in the engineering industry [4][5][6].
Notwithstanding the huge improvements achieved, a number of limitations still exists in the design of turbomachinery components. In fact, CFD-based optimizations allow to find the shape resulting in the best efficiency from a fluid dynamic point of view. However, this can lead to the obtainment of complex, non-manufacturable geometries with structural issues. For example, the thinning of turbomachinery blades to reduce losses might often result in excessive vibrations and deformations from a structural point of view. Therefore, the implementation of structural analysis already at an early stage of the design of such components would have a number of benefits, among which gathering of important information regarding manufacturing feasibility, part life and a possible reduction in time to market.

The field dealing with the interaction between structure and fluid dynamic is called *Aeroelasticity*. This concerns the relations between inertial, elastic and aerodynamic forces as described by Collar in the triangle of forces [7]:

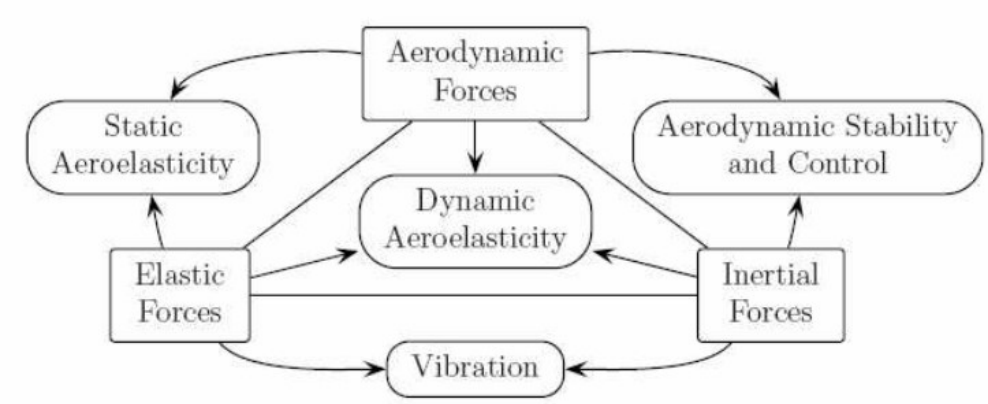

Figure 1.1: Aeroelasticity triangle of forces [7].

Although the implementation of dynamic aeroelasticity analysis in a shape optimization framework would provide invaluable information, it is highly unpractical. This is due to the extreme computational time that a high number of unsteady simulations would require. However, an optimization considering the interaction between fluid and structure in the steady state realm would still provide useful information, without a huge increase in computational time. This idea is at the base of the present research project.
A number of studies have been previously carried out on this topic. To mention one, Mueller et al [1] performed a multi-objective multidisciplinary optimization applied to a radial turbocharger for the automotive industry. This study found an improvement on both the total-to-static efficiency of the component, as well as the moment of inertia of the impeller. This, while simultaneously monitoring the stresses of the part, resulting in a mechanically viable solution. Moreover, Verstraete et al [8] also tackled this topic, creating a multidisiplinary design framework in which stresses were considered. This analysis is based on two levels, first the design space is investigated using a fast, but less accurate artificial neural network (ANN). Next, the best candidates are evaluated with FEA and CFD simulations to verify the previous prediction. This is further used to improve the accuracy of the ANN method. This framework was implemented on a micro radial compressor and showed that the stresses on the component can be drastically reduced with only a slight worsening of performances.

1.1. Thesis Motivations

As mentioned, one of the main limitations of the general design methodology for turbomachines nowadays is the lack of information gathered regarding the structural behaviour of the part already in the design phase. In fact, the most common design work-flow reckons on low-order preliminary design methods to determine an initial guess design, and follows with CFD-based optimization. The structural integrity and manufacturing feasibility of the part are then verified only retrospectively [9][10][11] by means of Finite Element Analysis (FEA) and ”hot-to-cold” transformation respectively. Here, the concept of ”hot” geometry refers to the desired shape of the part during operation, therefore when this is deformed under all the thermal and mechanical loads. On the other hand, as ”cold” design is intended the ”as-manufactured” shape, before

any load is applied. It is generally important to inspect the differences between these two geometries since turbomachinery components are often subject to high pressure, thermal and centrifugal loads, which might deform the part significantly from its initial shape.
According to the sequence just described, the mechanical assessment of the part is generally performed on the already optimized, ”hot” geometry. Moreover, once the structural viability of the part is verified under nominal loads, the ”hot-to-cold” transformation is performed. At this point, if the ”cold” geometry is found to be feasible from a manufacturing point of view, this design cycle stops and the part is either produced or further analyses on the off-nominal performances and unsteady structural behavior are performed. However, in the moment in which the optimum geometry is found to be either not mechanically viable, or unfeasible from a production point of view due to his complex shape, a new ”hot” geometry needs to be found. This in turn requires an additional design iteration in which all the above operations are to be performed once again, until convergence to a final feasible solution is reached. The aforementioned process can be extremely time-consuming and, above all, can lead to greatly sub-optimal solutions.
Instead, when including the structural ”cold-to-hot” transformation in the CFD optimization framework to make it a multidisciplinary study, it is possible to find a design that satisfies both manufacturing constraints and mechanical limits of the part in one single iteration, resulting in substantial time savings and possible improvement of the component’s performances.
To mention one, the Propulsion and Power Department of TU Delft already experienced such an issue. In fact, in previous years the department designed a radial inlet turbine (RIT) rotor for mini-ORC applications. This design, which can be found in [12] and is partly described in section 3.3, was performed in order to be implemented in the ORCHID [13]. This is an experimental test facility already present at TU Delft for the study of real gas behaviour in supersonic radial turbine for ORC applications. However, the design obtained resulted to not be manufacturable due to the excessively thin blades and the miniaturized nature of such component, making the production of such part quite challenging. Moreover, it was noticed that due to the high centrifugal loads the turbine is subject to, the blade deformations were high enough to make it impossible for the designer to neglect them. The requirement for a second design iteration of such turbine, starting from the already existent design previously obtained, and the need of a design methodology taking in consideration manufacturing constraints during the design process itself, rather than being just verified retrospectively, are at the base of the present research project.

1.2. Objectives and Research Questions

It is important to make a distinction to better clarify what are the goals of this research work:

- From an *engineering* point of view, this thesis aims to achieve a feasible optimized design for the ORCHID 10kW mini-turbine impeller, generating a trade-off between different suitable manufacturing methods and materials.

- From a *research* point of view, the goal of the present work is to demonstrate the suitability of a multidisciplinary design method to facilitate the trade-off on manufacturing methods and to reduce computational resources in the design of highly efficient, highly loaded radial impellers.

To sum up, the goal of the thesis can be outlined as:

This thesis work aims at creating an optimization framework where manufacturing constraints can be considered already during the design process.

The author aims to achieve this goal by implementing structural simulations in the design process in the form of Fluid-Structure Interaction (FSI) simulations. This is done by optimizing the *cold* geometry, to achieve the highest efficiency at nominal operating conditions, hence when the geometry is deformed by the loads (or *hot* geometry). In practice, this can be done by using the undeformed design as first-guess geometry for the optimization framework, for each optimization step perform first a ”cold-to-hot” transformation, and only then carry-out a steady-state CFD simulation to evaluate the performances. On the other hand, off-design performances and detailed unsteady aeroelasticity analysis of such turbine are out of the scope of the current thesis.
In order to test the methodology developed under this thesis work, the aforementioned ORCHID mini-turbine is used as test case.

Research Questions
The implementation of the methodology described above on a suitable test case, which will be thoroughly described in the following, will make it possible to answer the following research questions:

Q 1 What is the maximum efficiency attainable for the 10kW Radial Inlet Turbine under study when considering manufacturing constraints?

- **Q 1.1** How much is the impact of steady elastic deformation on aerodynamic efficiency?
- **Q 1.2** What are the main differences in terms final geometry when structural deformations are considered in the design process?
- **Q 1.3** How much additional computational time is needed when structural transformation is included in the design process?

Q 2 What are the consequences resulting from the implementation of the proposed design method on the trade-off between aerodynamic efficiency and technical feasibility?

- **Q 2.1** How do the results obtained affect the decision on the most suitable manufacturing method for the turbine under study?
- **Q 2.2** What are the circumstances in which the proposed method provides the best advantages?

1.3. Thesis Outline

The current thesis work is structured as follow. In chapter 2 the numerical methods at the base of structural and flow simulations performed and their coupling are explained, as well as the general structure of a surrogate base optimization and the specific algorithms employed. The test case studied with the proposed optimization method and the main characteristics of the turbine under study are then described in chapter 3. Next, in chapter 4, the actual framework of the optimization is presented, with details about the simulations performed and the validation of the assumptions made. Subsequently, the results of the different optimizations performed and a trade-off between different cases are given in chapter 5. To conclude, conclusions directly flowing from the results presented are shown in chapter 6, as well as shortcomings of the described method and possible future outlooks.

2

Numerical Methods

This chapter aims at presenting the main numerical models employed to perform the present thesis work. In particular, section 2.1 introduces the reader to the concept of Finite Element Method and gives some basics of elasticity theory for static applications. Subsequently, in section 2.2, the fluid dynamics equations of motions are presented with particular focus on the non-linearity of Navier-Stokes equations and how they are modelled in Computational Fluid Dynamics. Next, section 2.3 presents a general overview of what a fluid-structure interaction analysis is, going more in depth with the specific coupling method used in this thesis. To conclude, the general structure of a Surrogate Based Optimization is briefly explained in section 2.4, with details regarding the algorithms employed.

2.1. Structural Solver

To better understand how the displacements are evaluated starting from the applied loads, the theory behind the structural simulations performed is briefly touched upon in this section. Firstly, a general overview on what is the Finite Element Method (FEM) is given. Subsequently, details regarding the theory of elasticity are provided.

Finite Element Method

The Finite Element Method (FEM) is a procedure to numerically solve equations describing the behaviour of a certain phenomena [14]. When this method is used for static structural analysis, it comes down to the evaluation of displacements, stresses and strains of a solid body, and properties derived from these, when certain loads are applied. In the specific case of structural FEM, the equations dealing with isotropic materials when no thermal stresses are considered are conceptually quite simple, as will be shown later. However, the formulation of those relationships are based on conventions valid for simple shaped geometries that can not be directly applied to complicated 3D geometries.

In FEM, when a more complicated geometry is to be studied, this is discretized in a series of far smaller and simpler *finite elements*, forming what is called *computational grid* or *mesh*, making the numerical solution of the equations possible on each finite

element [14]. This allows the resolution of the equations describing the structural behaviour of a certain part, regardless of the complexity of its shape, or the presence of geometry or material non-linearities.

Theory of Elasticity
Generally speaking, the theory of elasticity is a branch of the continuum mechanics field focusing on the evaluation of deformations and stresses a solid body undergoes when prescribed loads are applied.
First of all, it is important to present some important definitions to know when speaking about theory of elasticity [15][16]:

- *Deformation:* refers to the change of a geometry when forces are applied. A solid body can undergo an *elastic* or *plastic* deformation, with the main difference being that the former describes a deformation where the solid goes back to its initial shape once the forces applied are removed, whilst the latter keeps part of them, resulting in a permanently deformed shape.
- *Displacement:* represents the vector quantity indicating the movement of a single point of the geometry when a force is applied on the solid body. Being it a vector, it can be represented based on its three components in the directions of the Cartesian axes:

$$\mathbf{u} = [u, v, w]^T \tag{2.1}$$

- *Strain:* refers to a vector quantity composed by 6 components:

$$\boldsymbol{\epsilon} = [\varepsilon_x, \varepsilon_y, \varepsilon_z, \gamma_{xy}, \gamma_{xz}, \gamma_{yz}]^T \tag{2.2}$$

  They are described as spatial partial derivatives of the displacements (or a combination of those). Each component is defined as:

$$\begin{aligned} \varepsilon_z = \frac{\partial u}{\partial x} \quad ; \quad \varepsilon_y = \frac{\partial v}{\partial y} \quad ; \quad \varepsilon_z = \frac{\partial w}{\partial z} \\ \gamma_{xy} = \frac{\partial u}{\partial y} + \frac{\partial v}{\partial x} \quad ; \quad \gamma_{xz} = \frac{\partial u}{\partial z} + \frac{\partial w}{\partial x}; \quad \gamma_{yz} = \frac{\partial v}{\partial z} + \frac{\partial w}{\partial y} \end{aligned} \tag{2.3}$$

- *Stress:* describes the internal resistance of a solid element due to loads. The stress vector is presented as:

$$\boldsymbol{\sigma} = [\sigma_x, \sigma_y, \sigma_z, T_{xy}, T_{zz}, T_{yz}]^T \tag{2.4}$$

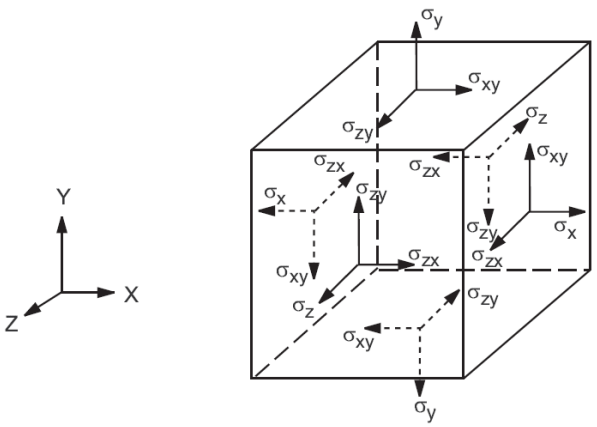

Figure 2.1: Stress components on a generic cube [16].

Both the strains and the stresses can be divided in 3 normal components and 3 tangential ones. In Figure 2.1 the sign convention for these vectors is presented for clarity. When initial strains and stresses are not considered, and thermal effects are neglected, the relationship between these two vector quantities is relatively simple, and it can be described as [14]:

$$\boldsymbol{\sigma} = \mathbf{D}\boldsymbol{\epsilon} \tag{2.5}$$

where $\boldsymbol{D}$ is the isotropic constitutive matrix, defined as:

$$\mathsf{D} = \frac{E(1-\nu)}{(1+\nu)(1-2\nu)} \begin{bmatrix} 1 & \frac{\nu}{1-\nu} & \frac{\nu}{1-\nu} & 0 & 0 & 0 \\ & 1 & \frac{\nu}{1-\nu} & 0 & 0 & 0 \\ & & 1 & 0 & 0 & 0 \\ & & & \frac{1-2\nu}{2(1-\nu)} & 0 & 0 \\ \text{Sym.} & & & & \frac{1-2\nu}{2(1-\nu)} & 0 \\ & & & & & \frac{1-2\nu}{2(1-\nu)} \end{bmatrix} \tag{2.6}$$

This shows as the strain-stress relationship for isotropic linear materials only depends on two material properties, namely the Young modulus E and the Poisson's ratio ν. Stresses and strains are then directly related to the loads acting on the 3D solid by means of the principle of virtual work (PVW) as:

$$\iiint_V \delta\boldsymbol{\varepsilon}^T \boldsymbol{\sigma} dV = \iiint_V \delta\mathbf{u}^T \mathbf{b} dV + \iint_A \delta\mathbf{u}^T \mathbf{t} dA + \sum_i \delta\mathbf{a}_i^T \mathbf{p}_i \tag{2.7}$$

where the component on the left-hand side of the equation is the internal virtual work of the solid body, whilst the right-hand one is the external virtual work. The latter is defined as summation of body forces, surface forces and point loads [14].

2.2. Fluid Flow Solver

Fluid dynamics is a branch of physics describing the behaviour of fluids when certain surface (e.g shear or pressure forces from a separate fluid or solid domains) or

body forces (e.g. gravity or rotational forces) are exerted. As for solid bodies, the conservation laws for mass, momentum and energy apply and they allow for the characterization of the properties of the fluid when its state is changed. Particularly, the motion of Newtonian fluids can be described by the conservation laws in a set of partial differential equations named Navier-Stokes (NS) equations.
This section aims to briefly describe the equations and assumptions laying the foundations of the CFD simulations employed in this thesis project.

2.2.1. Fluid Dynamics and Turbulence Fundamentals

For convenience, in fluid dynamics the flow is usually analysed as in a defined spatial region, using the so called *control volume (CV) approach*. This opposed to what is generally done in the study of the dynamic of solid bodies, where a *control mass (CM) approach* is employed [17]. The substantial difference is that the conservation laws are applied based on intensive quantities in the former (CM), and on extensive quantities in the latter (CV).
The three conservation equations previously mentioned, where only the assumption of Newtonian fluid is made, can be respectively seen in Equation 2.8, Equation 2.9 and Equation 2.10:

$$\frac{\partial \rho}{\partial t} + \nabla \cdot (\rho \vec{V}) = 0 \tag{2.8}$$

$$\frac{\partial (\rho \vec{V})}{\partial t} + \nabla \cdot (\rho \vec{V} \otimes \vec{V} + p\vec{I} - \overline{\tau}) = \rho \vec{f_{\varepsilon}} \tag{2.9}$$

$$\frac{\partial (\rho e)}{\partial t} + \nabla \cdot (\rho e \vec{V}) = -p \nabla \cdot \vec{V} + \epsilon + k \nabla^2 T \tag{2.10}$$

where τ in Equation 2.9 is defined as the strain rate [18].

In their general form, the Navier-Stokes equations do not have an analytical solution as of today, mainly due to their fully coupled time dependence, and the different non-linear terms. Since in this research project only steady state simulations were performed, the time coupling is not investigated further. On the other hand, the non-linearity of this system of equations needs to be studied in more details, with particular attention to the term $\vec{V} \otimes \vec{V}$ in Equation 2.9.
The non-linearity of the Navier-Stokes equation is mainly due to the presence of turbulence, and because of the compressibility of the fluid. Turbulent flows are highly unsteady, three dimensional with instantaneous property fluctuations in the time and all the spatial dimensions, and they are characterised by high vorticity. Moreover, they generally contains fluctuations with a wide range of time and length scales [19].
For real life applications, with varying Reynolds number, the range of length and time scales is in most of the cases too broad for the system of equations to be resolved analytically. Therefore, many efforts have been made and are still being made to model turbulence in simpler, less time and memory intensive ways.
Turbulence energy transition from large scale to small scale vortices can be described by the *turbulence energy cascade* [18]. This describes the process of generation of

turbulence in the form of large, also called integral, scale vortices, strongly related to geometry and flow boundary conditions. Next, the energy is transferred to medium, also called inertial, scale vortices and finally it is finally dissipated through micro scale eddies in the region of the dissipative scales, which are easier to model compared to the ones in the integral scale region. This principle is well depicted in Figure 2.2:

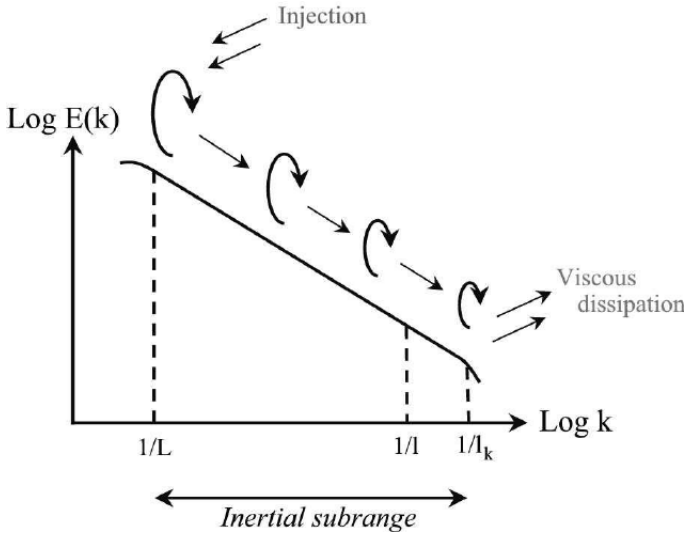

Figure 2.2: Turbulence energy cascade.

where the turbulent kinetic energy E is shown on the y-axis, whilst the wave number is used as x-axis. This last quantity is defined as shown below, and it contains fluctuating terms of velocity components (a differentiation of average and fluctuating terms is presented shortly):

$$k = \frac{1}{2}\left(\overline{u'^2} + \overline{v'^2} + \overline{w'^2}\right) \tag{2.11}$$

In the above image, the terms L (hereafter referred to as l_I) and l_K play an important role in the modeling of turbulence. They are called Integral and Kolmogorov length scales (respectively presented in Equation 2.12 and Equation 2.13), and mark the start and the end of the integral sub-range. Large eddies are generated at scales larger than l_I, whilst the dissipation mechanism is started for scales smaller than l_K.

$$l_I \propto \frac{k^{\frac{3}{4}}}{\epsilon} \tag{2.12}$$

$$l_K = \left(\frac{\nu^3}{\epsilon}\right)^{\frac{1}{4}} \tag{2.13}$$

where ϵ is the turbulent dissipation and ν the kinematic viscosity.

2.2.2. Computational Fluid Dynamics

In the previous section, it was mentioned that an analytical solution of the Navier-Stokes equations is impossible to obtain, apart for simplified specific cases. However,

it is possible to obtain ”approximate enough” solutions calculated numerically.
In Computational Fluid Dynamics (CFD), the system is described by the set of governing equations and boundary conditions applied, forming all together the mathematical model employed in the simulation. In order to do so, a discretization method is used to approximate the set of differential equations previously described into a system of algebraic equations for the different quantities, similarly to what happens in FEM simulations [19].
Of utmost importance is the decision of the model employed to describe turbulence. Among the most popular and used approaches, we find DNS, LES and RANS, where from the first to the last the grade of accuracy decreases more and more [17].
Direct Numerical Simulations (DNS) are the best method in terms of accuracy, where the Navier-Stokes equations are computed still by discretization, but with not other approximations or averaging. It resolves all the motions associated with turbulence. In this type of simulations, it is possible to capture the behaviour of the flow in the smallest eddies, so in the energy dissipation range. However, in order to do so a grid smaller than the Kolmogorov length scale is necessary, leading to very long computational times and making it prohibitive to use for real life applications.
Large Eddy Simulations (LES) are used to compute the larger length and time scales of turbulence, but modeling the motions belonging to the viscous sub-range. This allows the obtainment of less accurate results compared to DNS, but it strongly reduces computational time and it allows to widen up the applicability of CFD simulation.
Reynolds-Averaged Navier-Stokes (RANS) equations are probably the most used in industry for real life applications, allowing for a further reduction of computational costs, but at expenses of accuracy. Being this the method used for the entire research project, a separate section is dedicated to it.
The difference of length scales modelled, or solved, by these different types of CFD simulation is easily understood looking at Figure 2.3 , where also the energy cascade mechanism is displayed for easiness of visualization:

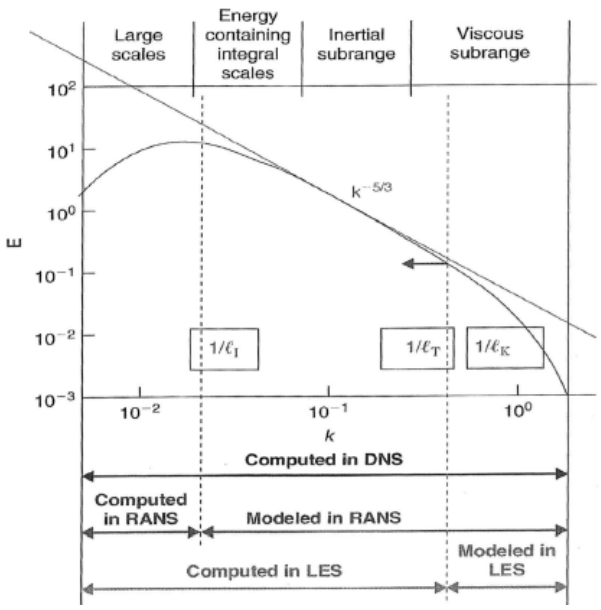

Figure 2.3: Scales modelled or solved by different CFD models [18].

Reynold-Averaged Navier-Stokes (RANS) equations
Simulations based on Reynold-Averaged Navier-Stokes equations are greatly used nowadays for engineering applications due to the relatively low computational time required. Moreover, in these applications the main interest is usually just toward few average quantities, making LES and DNS methods quite of an overkill.
When considering larger scale compared to the ones of turbulence fluctuation, the flow quantities can be with a good approximation be decomposed in an average and a fluctuating term:

$$u = \overline{u} + u' \tag{2.14}$$

This concept is called Reynolds decomposition and it is illustrated in Figure 2.4, where on the left it is shown for steady cases, whilst on the right for unsteady ones:

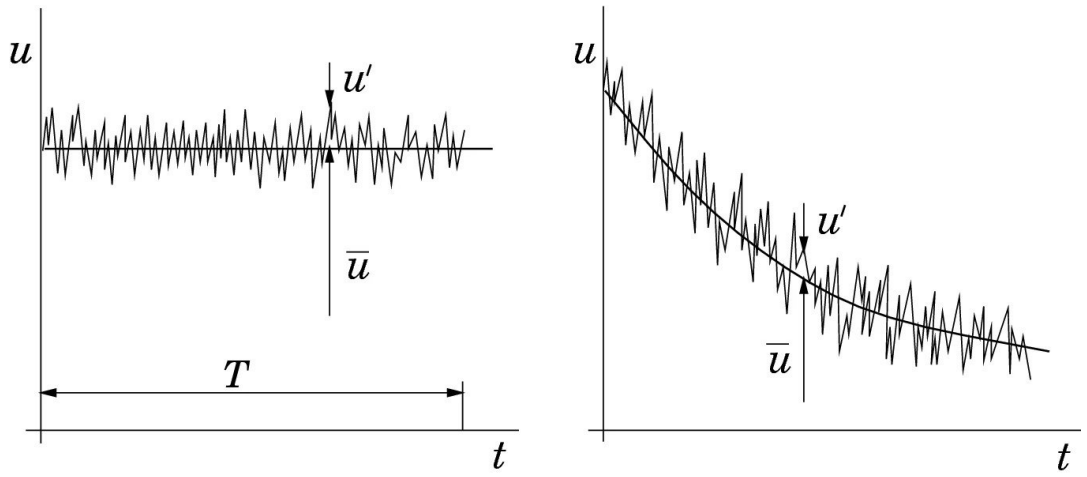

Figure 2.4: Time averaging of statistically steady flows (left) and unsteady flows (right) [19].

RANS equations are nothing but a form of the Navier-Stokes equations where Reynolds decomposition is applied. They allow to avoid the resolution of fluctuating terms, meaning that also the turbulence scales bigger than the ones in the viscous subrange are modelled.
When the Reynolds averaging is applied to Equation 2.8, Equation 2.9 and Equation 2.10, after some manipulations the Reynolds-Averaged Navier-Stokes equations are found (Equation 2.15, Equation 2.15 and Equation 2.17):

$$\frac{\partial \rho}{\partial t} + \nabla \cdot (\rho \vec{\overline{V}}) = 0 \tag{2.15}$$

$$\frac{\partial (\rho \vec{\overline{V}})}{\partial t} + \nabla \cdot (\rho \vec{\overline{V}} \otimes \vec{\overline{V}}) = \rho \vec{f_e} - \nabla \overline{p} + \mu \nabla^2 \vec{\overline{V}} + \frac{1}{3}\mu \nabla (\nabla \cdot \vec{\overline{V}}) - \nabla \cdot \left(\rho \overline{\vec{V'} \otimes \vec{V'}} \right) \tag{2.16}$$

$$\frac{\partial (\rho c \overline{T})}{\partial t} + \nabla \cdot (\rho c \overline{T} \vec{\overline{V}}) = k \nabla^2 \overline{T} - \nabla \cdot \left(\rho c \overline{T' \vec{V}} \right) \tag{2.17}$$

Because of their non-linearity, the averaging of the NS equations leads to the formation of new terms with products of fluctuating quantities that need to be solved using

specific models. In particular, the last term in Equation 2.16 is called Reynolds stress and it is defined as:

$$\overline{\overline{r}} = -\rho\overline{\vec{V}' \otimes \vec{V}'} \tag{2.18}$$

This is a symmetric tensor which combines velocity fluctuations:

$$\overline{\overline{r}} = -\rho \begin{bmatrix} \overline{u'^2} & \overline{u'v'} & \overline{u'w'} \\ \overline{v'u'} & \overline{v'^2} & \overline{v'w'} \\ \overline{w'u'} & \overline{w'v'} & \overline{w'^2} \end{bmatrix} \tag{2.19}$$

The presence of this term introduces an additional unknown that needs to be modelled by using one or more equations in order to ”close” the problem, leading to a further approximation of the system of equation. This is not unique, but different types of approximations can be made in order to achieve closure. Therefore, a *turbulence model* is to be chosen in order to obtain satisfactory results.

SST Turbulence Model

Turbulence models can be generally divided in: Eddy Viscosity Turbulence Models and Reynolds Stress Turbulence Models. Whilst the former assumes that the Reynolds stresses can be considered as proportional to the gradients of the mean velocity, the latter evaluate the transport of Reynolds stresses. Since in this thesis work the Shear Stress Transport (SST) model is employed, which is based on the eddy viscosity hypothesis, only this type of models is described in the following.

The Reynolds stress tensor can be regarded as the summation of an isotropic term and a deviatoric, anisotropic one:

$$\overline{\overline{r}} = -\rho\frac{2}{3}k + \overline{\overline{a}} \tag{2.20}$$

In this context, the Boussinesq’s hypothesis, shown below is of major importance.

$$\overline{\overline{a}} = \overline{\overline{r}} + \rho\frac{2}{3}k = -2\mu_T\overline{\overline{D}} \tag{2.21}$$

This means that a proportional relation can be drawn between the Reynolds stresses and the mean strain rate. The proportional coefficient μ_T is defined as *Eddy Viscosity*. Similar approach can be followed for the turbulent heat flux in the Reynolds-Averaged energy conservation law. in this case applying what is called the *Eddy Diffusivity* k_T :

$$-\rho c\overline{T'\vec{v}} = k_T\nabla\overline{T} \tag{2.22}$$

Therefore, in order to close the system of RANS equations when the turbulent heat fluxes are disregarded, the eddy viscosity and diffusivity terms are to be modeled.
Two-equations models are among the most popular ways of modeling the turbulence viscosity term just described. These make use of two different transport equation in order to evaluate the velocity and length turbulence scales from kinetic energy and another term. This term differs for different models and it can be the dissipation rate or the turbulent frequence, them being respectively ϵ and ω.

In order to evaluate the kinetic energy, a balance equation is to be evaluated, and this can be done by reworking the RANS equations, obtaining:

$$\rho\frac{\partial\kappa}{\partial t}+\rho\overrightarrow{\vec{V}}\cdot\nabla\kappa=\vec{r}:\nabla\vec{V}-C_D\rho\frac{\kappa^{g/2}}{l_T}+\nabla\cdot\left(\left(\mu+\frac{\mu_T}{\sigma_k}\right)\nabla\kappa\right) \tag{2.23}$$

where l_T is in this case defined as mixing length.
However, a second transport equation is needed to find the second unknown. The well known $\kappa-\epsilon$ [20] model and $\kappa-\omega$ [21] models are at the base of the SST turbulence model, one solving the equation for the turbulence dissipation, whilst the other doing so for the specific dissipation rate. These two models are widely used in CFD, but they both have few shortcomings. In particular, the first one tends to accurately predict the free-stream quantities, but fails in doing so for near wall regions, leading to the need of wall functions. On the other hand, the second one does not need any wall treatment, but being less accurate in mean flow regions.
The SST turbulence model [22][23] achieve an optimal combination of the two previously described models. In fact, it introduce an additional term, called blending factor, to vary the behaviour of the model between a $\kappa-\epsilon$ and a $\kappa-\omega$, depending on the position with respect to the wall.

2.3. System Coupling

The field of aeroelasticity deals with the coupling between structural behaviour of a certain part and the fluid dynamics behaviour of the flow around it. This field mainly considers three types of forces in what is defined the aeroelastic triangle of forces: inertial, aerodynamic and elastic force [7]. In the current research project, only static aeroelasticity is dealt with, meaning that the inertial forces are not considered, and the problem comes down to a coupling between the remaining two types of force.
Fluid-Structure Interaction (FSI) methods deal with the coupling of fluid dynamics forces and structural displacements, and they can be categorized in *monolithic approaches* and *partitioned approaches* [24]. Whilst the first one resolves the fluid dynamics and the structural problem simultaneously, combining them in a single problem, the second deals with the two problems separately and information are shared between the two fields during intermediate steps. In this chapter only partitioned approaches are analysed further due to their use in the current work.
The partitioned methods can be further divided based on if the information shared between the two fields is mono-directional or bi-directional [25]. These two sub-divisions are defined as:

- One-way coupling: the transfer of information only takes place in one direction. For example, in many cases the information is shared from the fluid dynamics to the structural field, in order to evaluate the pressure loads acting on a surface when studying its possible failure modes. A clarifying example of a possible one-way coupling workflow is shown in Figure 2.5.
- Two-way coupling: the transfer of information happen in both ways. Therefore, at every iteration the information is shared between both fields of interest. Also in this case, a possible workflow for such approach is shown in Figure 2.6.

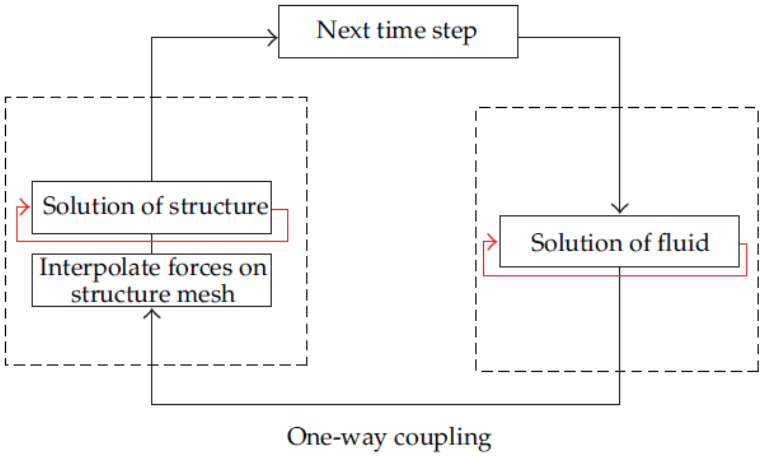

Figure 2.5: Example of one-way coupling workflow [25].

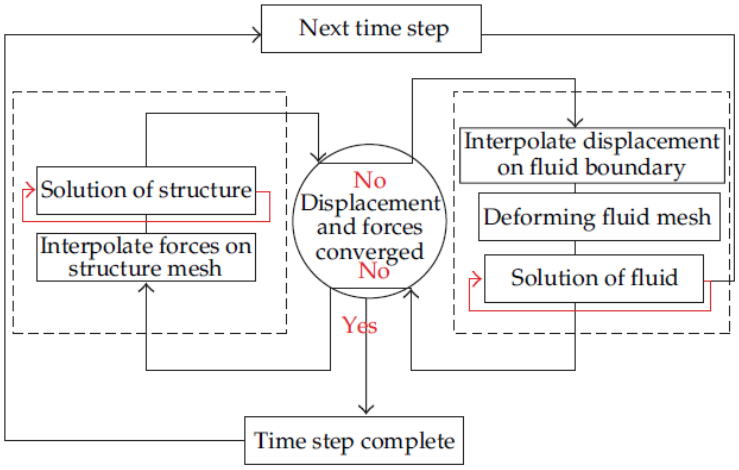

Figure 2.6: Example of two-way coupling workflow [25].

Data Transfer

The way in which the data is transferred between fields is critical for FSI analysis. The information are shared between the two systems at an interface between fluid and solid domains, that most certainly have different meshes. Therefore, a data transfer algorithm is needed in order to share quantities between different fields.
Data transfer algorithms include certain steps:

- *Data Pre-Processing:* in this step algorithms are employed to generate additional data on the interface between different fields. These data are then used for mapping or interpolation purposes.
- *Mapping:* as the name suggests, this step deals with the mapping of data location to allow for the exchange of information at the interface. For the current thesis work, the *Bucket Surface* is employed.
- *Interpolation:* at this stage the information is shared to the target node. This is done taking in consideration the additional data found in the first step, and the weight defined by the mapping algorithm.

- *Interpolated Data Post-Processing:* this step is mainly needed when there is necessity of post-processing in the interpolated data before exposing it to the other coupled field.

Particular attention needs to be given to the mapping algorithm. In Figure 2.7 it is possible to see a conceptual example of a simple Bucket Surface algorithm:

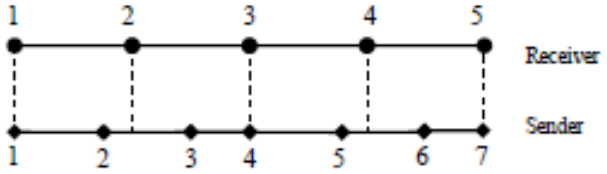

Figure 2.7: Bucket Surface explanatory example [26].

The Bucket Surface algorithm maps the mesh nodes at the interface of the target participant into the elements of the source participant. The first step is to source grid into a fictional structured mesh. All the the elements in this imaginary mesh are named ”buckets”. Next, the nodes on the grid surface of the target participant are related to one of those regions. After this, the algorithm computes the weights used for mapping by analysing the data contained in each bucket of the receiver participant.

2.4. Surrogate-Based Optimization

The goal of this section, is to provide the reader with enough knowledge regarding Surrogate-Based Optimizations to be able to understand the optimization framework carried out in this thesis project, which will be explained in detail in chapter 4. Since a number of different methods and algorithms can be used for different steps of the optimization, only the methods used for the current research project will be investigate further.

A Surrogate-Based Optimization (SBO), or Response Surface Optimization (RSO), is an optimization method particularly useful when the objective function to be evaluated is computationally expensive. In fact, this type of optimizations is based on the iterative generation, verification and, if needed, update of a surrogate model (SM), or response surface (RS), that represents ”accurately enough” the objective function to be optimized. This allows to perform optimizations where a much smoother and fast-to-evaluate surrogate is queried, rather than the actual initial high-fidelity function [5][4].
The process to be carried out to perform a response surface optimization can be condensed in few steps, described as follows:

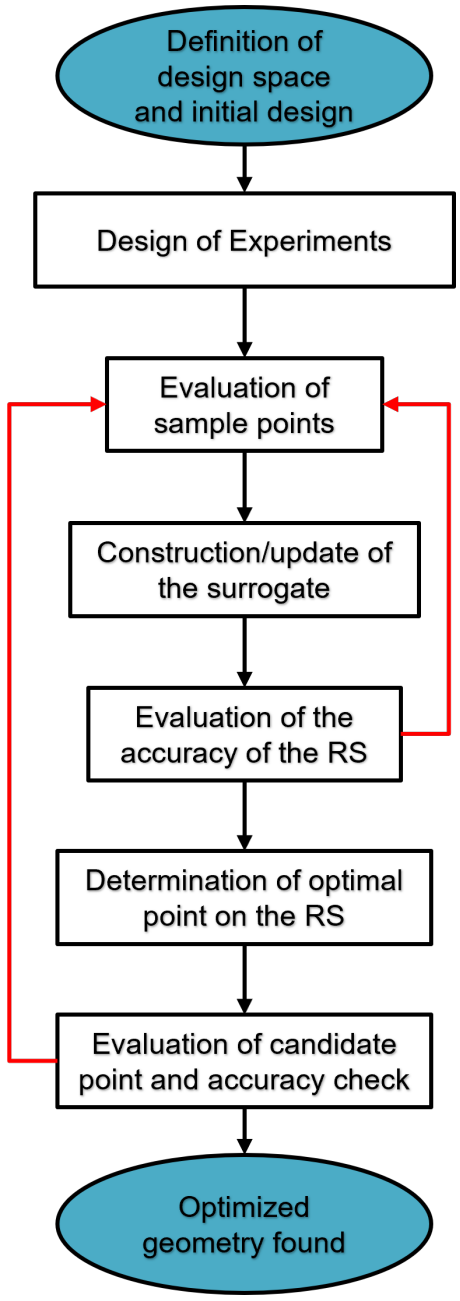

Figure 2.8: Surrogate-Based Optimization scheme.

1. At first a design space need to be defined, where a trade-off between computational time, accuracy and wideness of the space need to be addressed. In this part, the constraints, the function to be optimized and the design variables and their bounds are to be defined;
2. A Design of Experiments (DoE) is defined. This is a strategy to generate sample points over the design space, subsequently used to create the surrogate. Different types of DoEs exist and they have the objective to spread the sample points as widely and uniformly as possible throughout the design space, in order to obtain the most information with the least amount of points;
3. The sample points previously generated are evaluated;
4. A surrogate model is generated (or updated in case this is not the first iteration) by selecting a specific algorithm chosen with the aim of achieve maximum similarity between the response surface and the high-fidelity function;
5. The surrogate is checked for accuracy. If the accuracy is deemed not sufficient, more design points are added to create a better fit. Alternatively, a different surrogate model can be used that better interpolates the sample points evaluated;
6. An optimization is performed on the surrogate model to find the optimal point. Being the surrogate smoother and easier to evaluate than the first objective function, this optimization is carried out in relatively short time;
7. The candidate optimum is evaluated and its accuracy is checked. If the accuracy is satisfactory, an optimum is found, otherwise more points are added to the DoE (or a different surrogate algorithm is used).

2.4.1. Design of Experiments

Designs of Experiments, also just called sampling methods, are strategies to sample the design space with design points that are evaluated in order to create the first iteration of response surface, or surrogate model. This is usually the most time-expensive step in SBOs, due to the high number of evaluations of the objective function to be performed, evaluations that are generally quite lengthy, like in case of CFD based optimizations or experiments. For this reason, the design of experiments needs to be chosen carefully.
The sampling method and number of samples need to be selected according to the specific problem that is to be investigated, or optimized. In fact, according to the expected shape of the surrogate model sought, a different number of samples is needed. The ultimate goal of every DoE is usually maximizing the information gathered regarding the design space during the process of evaluation of the samples, but using the least amount of points to decrease computational time [4].
For this research project, the Optimal Space Filling (OSF) method, explained in more detail in the following paragraph.

Optimal Space Filling
In order to describe the Optimal Space Filling sampling method, we first have to introduce the Latin Hypercube Sampling (LHS) method. In fact, the former is tightly based on the latter, with an addition of post-processing to achieve optimal spacing between the candidate points [5].
Latin Hypercube Sampling is a popular sampling method that allows the sample points to be distributed efficiently in the design space. Once a number P of design points is chosen, the range of each design variable is divided in a number P of ”sub-ranges”. The algorithm then randomly places the sample points in the design space so that every subrange contains one, and only one design point. To give a better idea, let’s take a practical example. If we take a design space with only 2 design variables, and we want to insert 8 sample points, with LHS a possible sampling would be the one shown in Figure 2.9. As can be seen, the two variables, here represented as the two sides of the ”square” representing the design space, are divided in 8 parts, and each of them only contains one, and only one sample.

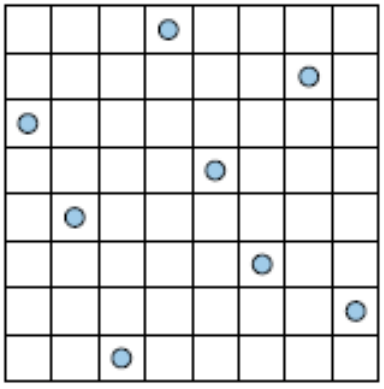

Figure 2.9: Example of a possible LHS sampling with 2 variables and 8 sampling points [5].

The one just explained is an efficient way to cover the ranges of the different design variables under study. However, this method doesn't come without shortcomings. For instance, the extremes of the space to be studied are not necessarily well covered, but particularly, this type of sampling method could still result in non-uniform samplings, by generating clusters of points. It suffices to think about a case where all the design points are on the diagonal of the square, the method is satisfied but the points are not spread as one would like.
The OSF method aims to alleviate these shortcomings. It optimizes the spread of the sample points through a post-processing and iterative process. Therefore, once a LHS scheme has been created, a second iteration is performed, in which another LHS design is found, but where the distance between points is optimized, with the goal of having the most uniform and spread distribution possible [27]. A sensible difference between these two methods is shown in Figure 2.10 and Figure 2.11. It can be seen that both sample schemes respect the requirements of an LHS method, but the one found with Optimal Space Filling appears more uniform. This allows the design space to be well covered with a lower number of points.

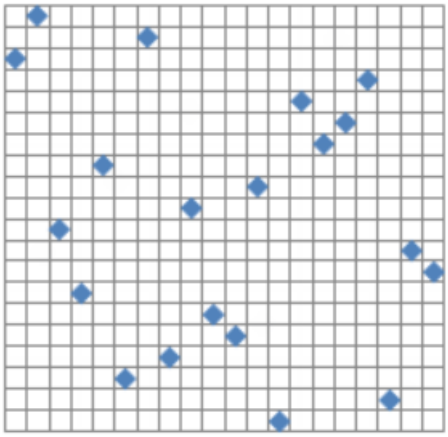

Figure 2.10: Example of sampling generated with LHS [27].

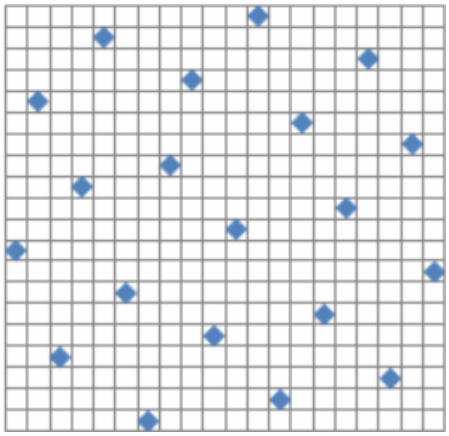

Figure 2.11: Example of sampling generated with OSF [27].

2.4.2. Surrogate Model

As surrogate modelling technique, Kringing has been used. This is one of the most popular methods to interpolate data used nowadays [6][28]. Particularly suited to build relations for highly non-linear functions, or simulations, Kringing works on the assumption that the response surface, or surrogate model, follows a Gaussian process [4][28]. This model approximates the objective function under study using a regression model and a stochastic process:

$$f(\boldsymbol{x}) = \boldsymbol{g}(\boldsymbol{x})^T \beta + Z(\boldsymbol{x}) \tag{2.24}$$

where the first term is the regression model, obtained from the product of a regression coefficient and a regression vector. Instead, $Z(\boldsymbol{x})$ is the stochastic process where a normally distributed Gaussian random process is built with zero mean, a process variance σ^2 and a non-zero covariance. On the one hand, the former is needed to

provide a general approximation of the function behaviour . On the other hand, the stochastic process is used to characterize the variation taking place locally [5][4].
The covariance matrix is described as:

$$\text{Cov}\left[Z\left(x^{(I)}\right) Z\left(x^{(J)}\right)\right] = \sigma^2 \mathbf{R}\left(\left[R\left(x^{(n)}, x^{(J)}\right)\right]\right) \tag{2.25}$$

where **R** is a correlation matrix and $R\left(x^{(n)}, x^{(J)}\right)$ is correlation function, describing the spatial relation of a function between any two sample points. In this case, this is a Gaussian correlation function as:

$$R(\boldsymbol{x}, \boldsymbol{y}) = \exp\left[-\sum_{k-1}^{\kappa} \theta_k \left|x_k - y_k\right|^2\right] \tag{2.26}$$

Here, θ are the unknown correlation parameters [27][4].

2.4.3. Surrogate Optimization

As explained in subsection 2.4.1, once the design space is sampled and the response surface, or surrogate model, is generated, it is possible to run a simple optimizer to find its optimum. For this step, the Non Linear Programming by Quadratic Lagrangian (NLPQL) is used. This is a single-objective optimization technique by Schittkowski [29] [27].
Many optimizers use general sequential quadratic programming algorithms to solve nonlinear constrained optimization problems [30]. These methods often use a line search following the direction found with the quadratic programming subproblem. The NLPQL methods uses a similar approach, but replacing the non-differentiable line search with a Lagrange function [30].

3

Test Case

This chapter aims to provide the reader with a context on the turbine used as study case for the current research project, and the different cases investigated. In order to do so, a short introduction on the ORCHID facility is presented in section 3.1. Subsequently, the initial design of the ORCHID turbine achieved in a previous thesis work is described together with its main features and requirements in section 3.2. To conclude, in section 3.3, an overview of the different cases investigated by means of the developed optimization framework is given.

3.1. The ORCHID

In the last years many research efforts have been put into improving the exploitation of renewable energy sources and wasted heat recovery.
In this context, the ORC applications, and more specifically mini-ORC technology, have been one of the focuses of the the Power and Propulsion group of TU Delft. At the time of writing, the department is working at the development of the ORCHID (Organic Rankine Cycle Hybrid Integrated Device) [13], see Figure 3.1. The ORCHID is a test facility that has been built in the last years at Delft University of Technology. Although the facility will consist of two different test sections, only one of the two is currently operational. On the one hand, a planar de Laval nozzle is already being used for experiments focusing on non-ideal compressible fluid dynamic. This section is already running and being used since 2019. On the other hand, a mini-ORC turbine is being developed with the main objective of studying the real gas behaviour in mini-ORC expanders. The device has been designed to operate in a wide range of operating conditions and will aid the generation of design guidelines for such applications. This will allow the obtainment of experimental data for validation of CFD codes and existing design methods, and to assess the correctness of loss models for compressible real fluids currently used. The design of such a turbine, starting from an already existent preliminary design performed in the past is at the base of the present research project.

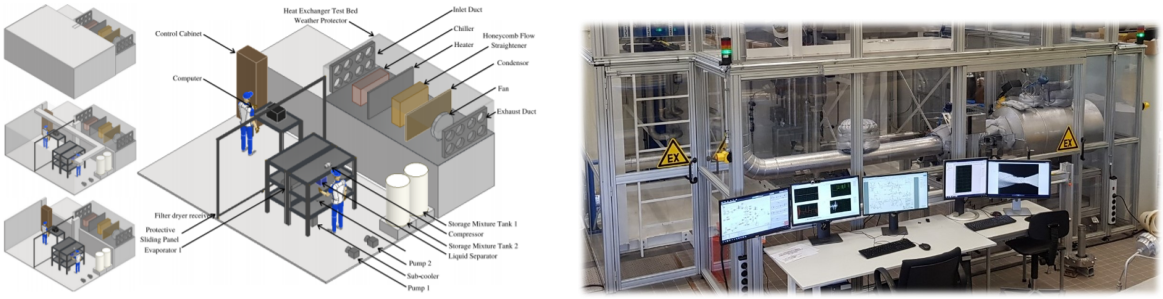

(a) Visual schematic of the ORCHID facility.

(b) Picture of the current ORCHID facility.

Figure 3.1: The ORCHID facility.

3.2. ORCHID Expander

The turbine under development for the ORCHID, and test case for the current research work, is a radial inlet turbine (RIT) composed of a single stage, including a vaned stator and a rotor.
This thesis focuses on the design of the ORCHID turbine rotor, whilst the design of the supersonic stator is outside the scope of this work. A picture of the initial design of such turbine is shown in Figure 3.2.
Siloxane MM (hexamethyldisiloxane, $C_6H_{18}OSi_2$) is the organic fluid employed to run the expander.

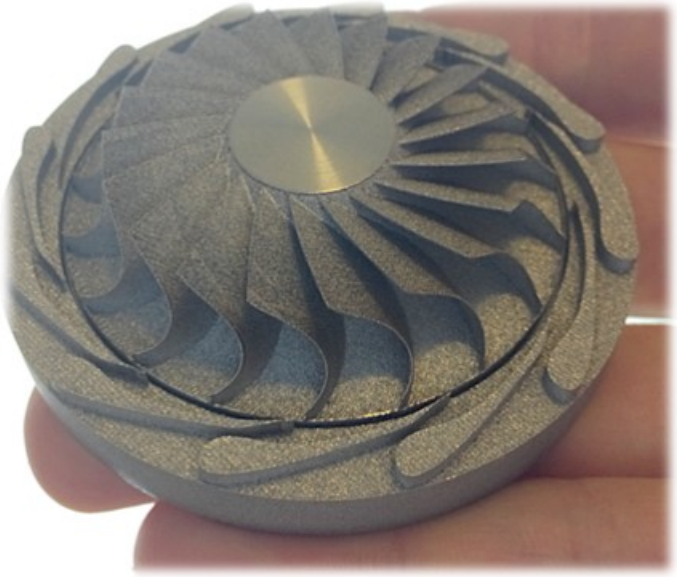

Figure 3.2: Picture of the first iteration of the ORCHID mini-turbine design manufactured with metal 3D printing.

From the first design iteration performed on the turbine, the main flow and turbine characteristics are found, see Table 3.1:

Table 3.1: Main expander parameters.

Input parameters	
Turbine architecture	RIT
Working fluid	MM
Mass flow	$0.1315\ kg/s$
Rotational speed	$98119\ rpm$
Stator inlet total temperature	300.0 C$^\circ$
Stator inlet total pressure	$18.093\ bar$
Rotor outlet static pressure	$0.443\ bar$

On the other hand, the main geometrical features of stator and rotor are presented in Table 3.2. The parameters reported in the following table are fixed, meaning that will not be modified during the optimization process.

Table 3.2: Main expander geometrical features.

Geometric parameters	Stator	Rotor
Inlet radius	$34.8\ mm$	$25.7\ mm$
Inlet to Outlet radius ratio	1.3	1.795
Inlet blade span	$2\ mm$	$2\ mm$
Outlet blade span	$2\ mm$	$12.3\ mm$
Inlet to Outlet height ratio	1	5
Normal tip clearance	-	$0.2\ mm$

where the outlet rotor radius is meant the radius at mid span section.
The expander features a supersonic stator, with convergent-divergent vanes. The design of this is done by means of an external tool which employs the Method of Characteristics tailored for this application. However, the design method for the stator is not presented since this thesis focuses on the design of the turbine rotor. During the optimization this part will be kept unchanged.
Three of the twelve stator blade profiles are shown in Figure 3.3 for clarity, where only the contours are provided since the blade profile is constant over the span.

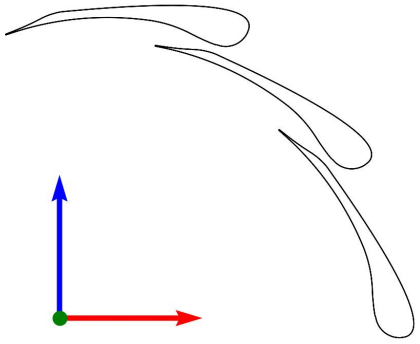

Figure 3.3: Contours of a 3 stator blades set.

3.3. Study Cases

In order to study the manufacturability of the ORCHID turbine impeller and to guide the decision on what manufacturing method is the most suitable for it, a trade-off is necessary. Due to the high computational cost of CFD-based optimizations and to time constraints, a low number of combinations of manufacturing method and material can be investigated.
In this section, the manufacturing methods studied are described, with some details regarding the constraints directly coming from them. Subsequently, the materials considered and their main properties are presented.

3.3.1. Manufacturing Methods

After a broad literature study on existing manufacturing methods, mainly focused on those applicable to turbo impellers, only two of them were selected. The manufacturing methods investigated in this thesis are additive manufacturing and CNC milling. The driving factors for the decision were mainly their popularity, and hence the existing knowledge on the methods, its applicability to miniaturized parts and the existence of contacts between the department and possible suppliers.
To give an example, investment casting has arguably been in the past years one of the most common manufacturing methods for turbomachinery impellers. However, it is not particularly suited for miniaurized parts and it does not feature a particularly high accuracy. Moreover, one of its biggest advantages is that it is low cost and fast for large volume production. Despite said advantages, the prototype nature of the ORCHID turbine development project makes the adoption of casting economically and technically unattractive. On the other hand, Electro Discharge Machining (EDM) and Electro Chemical Machining (ECM) are unconventional machining methods that have been getting increasingly popular. This because of the high geometrical accuracy and the superior surface finish attainable. However, the higher equipment and process costs make the latter methods comparatively more expensive and less accessible.

One of the most popular manufacturing methods for realizing complex, three-dimensional

shapes while retaining good surface finish and geometrical accuracy, is the widely diffused 5-axis CNC milling. Thanks to the high flexibility of this technology, and its large diffusion, which makes it a relatively cheap choice for rapid prototyping, TU Delft Power and Propulsion department previously investigated its use for the realization of the ORCHID turbine's impeller. However, the extremely demanding geometrical characteristics of the initial impeller design [12] called for an important redesign, leading to reduced blade count from 19 to 11 (more details on this are presented in subsection 4.1.2) and increased blade thickness. Although the shape optimization was performed with increased blade thickness, the minimum threshold was set from 0.2mm to 0.6mm for the blade tip, the achievement of high geometrical accuracy on the final part is still very challenging. This is due to the high forces at play during the cutting process of high performance materials, such as those required by this application.

Regarding additive manufacturing, a prototype of the turbine under study has already been printed by an external company. The technique employed was Selective Laser Melting (SLM) with an EOS M 290 printer. After some iterations, the provider was able to print an impeller with blade tip thickness as low as almost 0.3mm, but due to the number of iterations required and the risk of getting inaccurate tolerances, 0.4mm was used as a minimum threshold for the optimization when 3D printing is employed. There are no strong constraints in terms of blade number in this case due to the nature of additive manufacturing. However, an overhanging constraint needs to be implemented. This is defined as the minimum angle between the blade surface and the built plane. Therefore, a constraint on the overhanging being higher than 23 degrees everywhere on the blade surface was applied to the optimization upon successful manufacturing of such overhang for this specific design. In Figure 3.4 two turbine iterations are presented, one who failed due to mechanical stresses and the final successful one. The turbine in the picture is with reduced blade thickness as mentioned before.

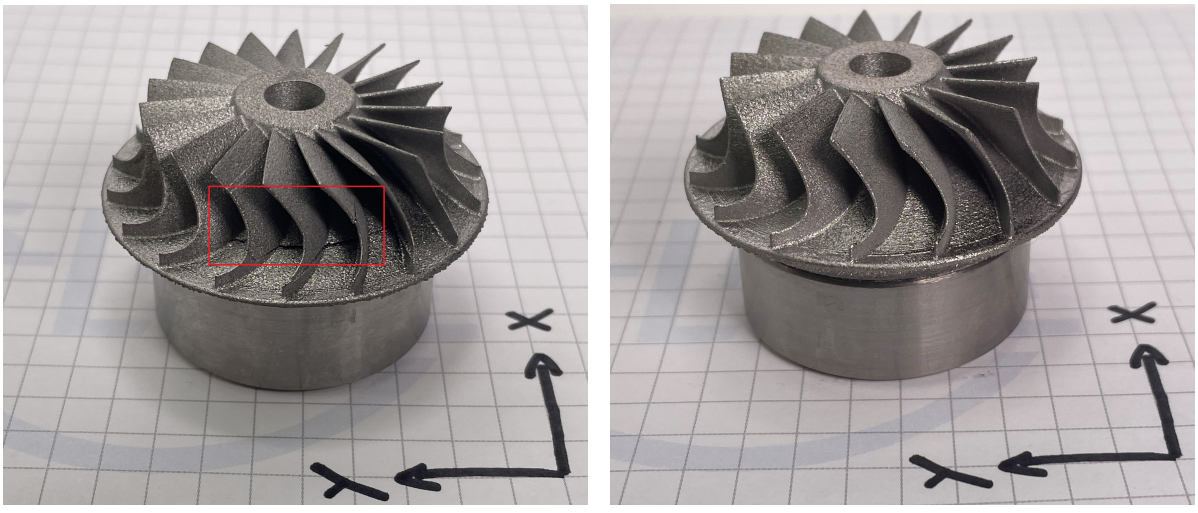

(a) First iteration of the prototype with cracks at the hub.

(b) Final iteration of the prototype with no cracks.

Figure 3.4: ORCHID turbine prototype manufactured with SLM.

3.3.2. Materials

Regarding the materials, the cases under study are titanium (Ti-6Al-4V) and stainless steel (316L). An overview of the main material properties at $250°C$ (temperature of the blades assumed to be the same as the flow main temperature) can be found in Table 3.3:

Table 3.3: Main material properties used for titanium and stainless steel.

Material	Density	Young's modulus
Ti-6Al-4V	$4374\ kg/m^3$	$96.61\ GPa$
Stainless steel 316	$7850\ kg/m^3$	$183\ GPa$

There are several reasons why these specific materials were chosen.
Ti-6Al-4V is a high performance titanium alloy grade, widely used across various industries. In particular, its high performances at relatively high temperatures (such as those reached in a mobile ORC machine), makes it attractive when compared against high performance, aerospace grade aluminum alloys. Moreover, a study on the original design of the ORCHID turbine impeller showed that the material provides satisfactory safety factors both under static and dynamic loads [31]. The increase of blade thickness implemented in this second design iteration increases still more the safety factors previously evaluated in terms of mechanical resistance.
The decision regarding stainless steel (316L) was mainly due to the confidence the CNC supplier has with machining such material, other than being one of the most common stainless steel alloys and having similar mechanical properties in terms of strength to titanium alloys. Moreover, stainless steel generally features higher strength compared to many other materials like aluminum or thermoplastic materials at the operating temperature (around $250°C$), and is commonly used in industry. The specific stainless grade used also features a young modulus almost twice as the on of titanium, meaning that no hugely higher deformations are expected with respect to its counterpart, despite its higher density.
In order to sanity check the materials chosen before the optimization, preliminary static structural finite element analysis (FEA) simulations were performed on the initial design of the turbine. Fillets were implemented to avoid stress singularities in this case. This showed that whilst the case with titanium features equivalent stresses well below the yield strength of the material, for the stainless steel the safety margin is far narrower.
The maximum value of stresses is as expected at the blade root, and its values are reported in Table 3.4 for stainless steel and titanium.

Table 3.4: Yield strength and maximum Von Mises stresses evaluated from preliminary FEA simulations[32][33].

Material	Yield strength	Maximum stress
Ti-6Al-4V	$570\ MPa$	$167.01\ MPa$
Stainless steel 316	$210\ MPa$	$201.31\ MPa$

A contour of the equivalent Von Mises stresses is shown in Figure 3.5 for the case with stainless steel. It is worth reiterating that the FEA was performed on a first iteration impeller and not on the final model used in the optimization with thicker blades. If anything, this should give more confidence in the materials used since the blades are in this case thinner than what has been used in the final simulations. Moreover, to still increase confidence in the use of such materials, the FEM simulations were performed for the material at $300°C$. In fact, the flow temperature is actually expected to be on average around $50°C$ lower. This means that the stresses evaluated are actually higher than the ones expected at operating temperatures, and also the yield strength of the material is decreased.
The fact that the stresses evaluated are below the yield strength of the material, even if mildly for the stainless steel case, together with all the conservative assumptions used, gave confidence that the materials chosen will withstand the operating loads. However, a more detailed structural feasibility study is required to also study the unsteady aeroelasticity effects on the impeller.

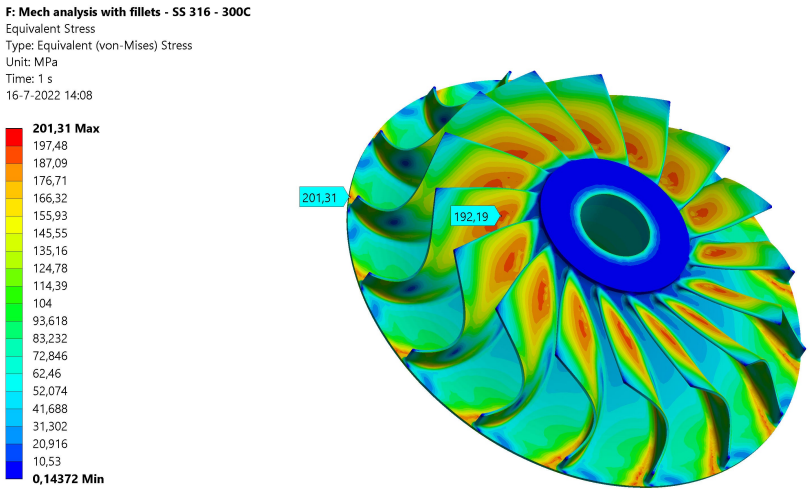

Figure 3.5: Contours equivalent Von Mises stress on the turbine.

4

Optimization Framework

In the following chapter, the setup of the optimization framework is presented. At first, the initial parametrization of the turbine is described in section 4.1, followed by information regarding the numerical grids and setups of the FEA and CFD simulations performed, respectively in section 4.2, section 4.3 and section 4.4. To conclude, in section 4.5 more data is provided regarding the detailed implementation of the surrogate based optimization, ranging from algorithms used (already mentioned in chapter 2) to number of simulations performed.

4.1. Initial Geometry and Parametrization

One of the first steps when setting up an optimization problem is the definition of the design variables, hence the geometry parametrization. This is done in order to vary the geometry to be evaluated during the optimization process.
In the present thesis project, mainly the blade angles and curvature have been studied as design variables, with some further information gathered in terms of blade number and thickness. Moreover, optimization of the meridional channel is not performed since this was done in the previous design iteration. The impeller geometry is defined, when the meridional channel is set, by the camberline shape over the span, the span-wise thickness distribution and the number of blades. The following paragraphs aim to give an overview of the parameters studied and the reasoning behind their decision.

4.1.1. Design Variables

The blade shape has been defined by specifying its thickness and camberlines only at the blade root and tip, whilst their span-wise variations are obtained from a simple linear interpolation of these parameters at the aforementioned locations. To give a better idea of how this is done, in Figure 4.1 the the different layers defining the shape of the blade are shown. In particular, the leading edge and trailing edge, together with the root and tip contours define the boarders of the blade, whilst the three lines visible inside the external contours are used to define the three-dimensional blade geometry and the variation of shape over the span. In the image below, these are shown as

sketch lines on the meridional plane of the blade, hence why they are not exactly aligned with the blade shape itself.

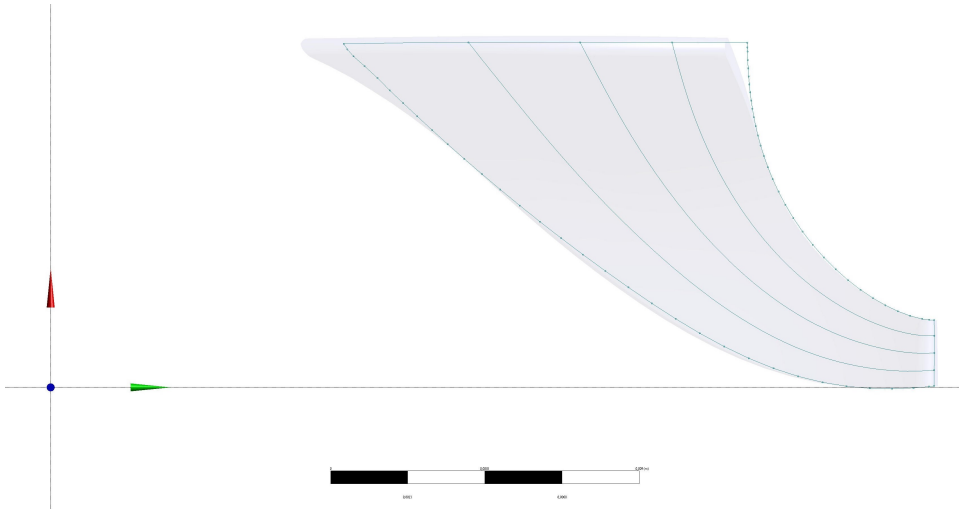

Figure 4.1: Blade shape seen in the meridional plane together with sketch lines defining its geometry.

In order to describe the hub and shroud camberlines, the blade angle β with respect to the meridional plane is used. This angle defines the three-dimensional camber line of the blade following the relation:

$$R \cdot d\theta = dm \cdot \tan(\beta) \tag{4.1}$$

where β is the blade angle, θ is the camberline circumferential position and dm is the infinitesimal meridional length in this case.
The distribution of β at root and tip is found by means of Bézier cubic polynomials using four control point, as shown in Figure 4.2, similarly to [1]. As already specified, the three dimensional distribution over the span is then obtained as linear superposition of these two curves.

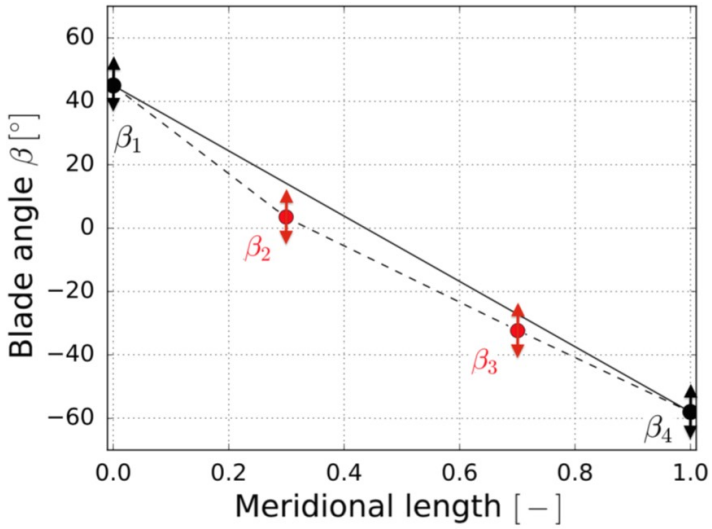

Figure 4.2: Camberlines parametrization.

In particular, the inlet and outlet angles β_1 and β_4 are kept constant spanwise for manufacturing easiness, and to not overcrowd the optimization problem with too many design variables. On the other hand, the angles describing the blade curvature β_3 and β_4 are independent at hub and tip to allow different span-wise curvatures on the blade.
An overview of the educated design ranges chosen for the optimization is found in Table 5.3, where x_i, x_{low} and x_{up} are the initial guess, lower bound and upper bound respectively:

Table 4.1: Educate range of design variables used in the optimziation.

Design variables	x_{low}	x_i	x_{up}
β_1	$37°$	$45°$	$53°$
β_4	$-61.2°$	$-57.2°$	$-49.2°$
$\beta_{2,hub}$	$-29.4°$	$-9.4°$	$10.6°$
$\beta_{3,hub}$	$-56.8°$	$-46.8°$	$-26.8°$
$\beta_{2,tip}$	$5.4°$	$25.4°$	$45.4°$
$\beta_{3,tip}$	$-96.1°$	$-86.1°$	$-66.1°$

It is worth to stress again that the values of β_2 and β_3 do not correspond to the actual blade angles, but only the control points used to define the corresponding Bézier curve.
As mentioned already, the initial guess is taken from the results generated in the first iteration of optimization of this turbine found in [12]. The bounds are relatively tight due to the fact that this is a second design iteration this turbine is undergoing, meaning that no excessive geometry changes are expected from the initial guess. The expected differences are mainly due to the structural transformation implemented, the change of number of blades from the former design which in turn affects the optimal slip angle and the increase in thickness derived from manufacturing constraints.

4.1.2. Number of blades

Response surface optimizations notoriously do not deal in an efficient way with discrete design variables. In fact, a discrete design variable is not just an additional variable to be added to the list, but it is handled by creating a different response surface for each discrete value in the variable range. It suffices to consider that a discrete variable with 8 different values considered in the optimization will increase its computational time by 8 times. This hugely increases the number of sample points to be evaluated to achieve the same accuracy as if the discrete parameter was not included, and it causes several surrogate algorithms to drop their auto-refinement capabilities. Due to the time constraints and the number of study cases to be studied, it was decided to not include the number of blades as design variable for the optimization framework.
However, the number of blades, which in turns defines the impeller solidity, have a

great impact on the performances of the turbine and the loading the different blades undergo. Moreover, being the thickness of the blade quite higher than the one studied in the previous optimization, it was expected that the optimal number of blades would have been quite different and lower than the previous case. To not fully disregard this aspects, a sensitivity analysis has been performed to study the behaviour of the efficiency at varying number of blades. The result of this study can be observed in Figure 4.3, where the different efficiencies are normalized using the maximum efficiency found:

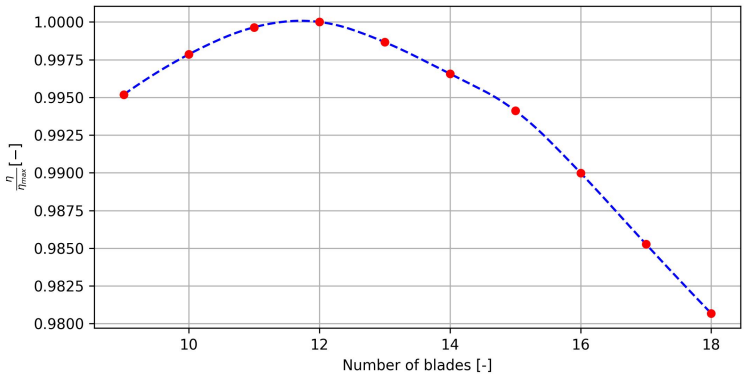

Figure 4.3: Total to static efficiency distribution when varying number of blades of the rotor.

The result shows that the best efficiency for the initial blade design is achieved for a number of blades of 12. However, the number chosen for the optimization is 11 due to the fact that it is usually avoided to use same number of blades for stator and rotor to not incur in excessive vibration and natural frequency issues.

4.1.3. Blade Thickness

Although the importance of such a parameter, the blade thickness has not been included in the optimization either. The main reason for its exclusion from this study is the time constraint and the clear trend observed in the previous simulations performed. In fact, differently from what was thought initially, the inclusion of the stator in the CFD simulations performed was deemed necessary only at a late stage of the project. This led to an increase in element number and hence the need to reduce the number of variables to limit computational time.

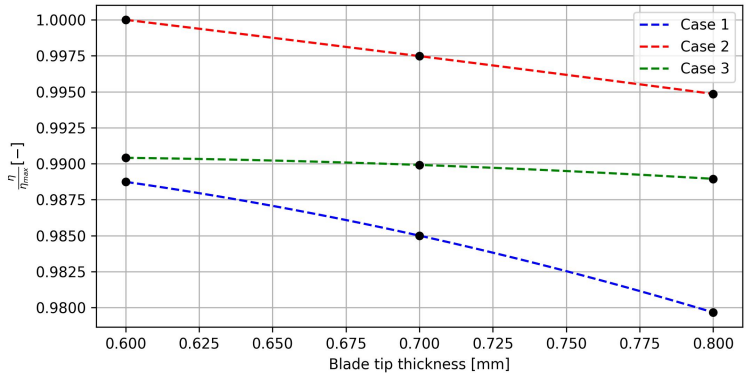

Figure 4.4: Total to static efficiency distribution when varying blade thickness for different blade geometries.

On the other hand, from the first simulations performed and the first iterations of optimization carried out featuring the stand-alone rotor, it has been noticed that a reduction of blade thickness was accompanied by an increase in efficiency. To further validate this trend, three different blade designs (with different outlet angles and blade curvatures) have been simulated at different thicknesses when also including stator. The results, shown in Figure 4.4, confirmed those assumption. In fact, although with different slopes, we can see a clear downward trend for every investigated case. Therefore, it was decided to fix the blade tip thickness to 0.6mm when optimizing the impeller for CNC manufacturing, and to 0.4mm for additive manufacturing, which are the lower boundaries of the previously considered variables dictated by manufacturing constraints.

4.2. Numerical Grid

In this section, the numerical grids, or meshes, employed for the FEM and CFD simulations are described, with some hints on how these were determined.

4.2.1. FEM Mesh

The computational mesh used to perform the FEM structural simulation only includes the blade, disregarding the influence of the impeller disk. It was generated using the standard ANSYS mesher tool.
It has been decided to only include one impeller blade for the structural simulations. This allowed a slight reduction of computational time, but particularly of computational memory for the optimization without affecting noticeably the results. In fact, it was noticed that the exclusion of the impeller hub disc from the simulations only resulted in a change of maximum deformation of about 5% at the outlet tip. Aside from that small region, the deformation on the rest of the blade seems to be negligibly affected by the presence of the hub.
Only the deformations are relevant for the current optimization framework, and an acceptable accuracy can be obtained quite easily in this regard with a restricted number of elements. Therefore, the mesh obtained is relatively coarse, with only 9000

elements. Although it would be certainly interesting to also study the behaviour of equivalent stresses during the parametric study, this would require the modelling of fillets to avoid stress singularities, that would in turn require a far more refined mesh. This would drastically affect the computational time and memory required for the optimization, and hence has not been investigated in the present work.

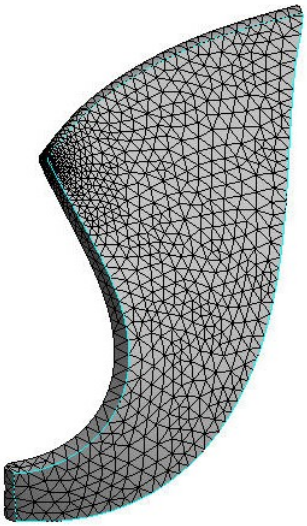

Figure 4.5: Mesh used for the FEM simulations.

The numerical grid features a refinement at the blade tip to better predict the deformations in that area, where the maximum occurs. Moreover, a brief convergence study was performed. In particular, two parameters were changed, the overall element size, and the blade tip element size, hereinafter respectively referred as l and l_{tip}. In Table 4.2, an overview regarding the numerical grid study performed is presented, where the third column, referred as Δdef, indicates the percentage of variation from the most accurate result, hence the one with l of 0.1mm and l_{tip} of 0.01mm. In this study, the aim was to obtain a mesh with a maximum deformation below 1% from the most refined mesh simulated.

Table 4.2: Mesh study for FEM simulations.

$l\ [mm]$	$l_{tip}\ [mm]$	Δdef [%]
0.1	0.01	0
1	0.1	-2.12
0.8	0.1	-1.59
1	0.08	-1.97
0.8	0.1	-1.40
0.6	0.1	-1.16
0.6	0.06	-1.06
0.5	0.08	-0.81
0.5	0.1	-0.86

It can be observed that a reduction of element size at the blade tip does not affect the results of the FEM simulations noticeably. However, due to its low impact on the mesh count, it has been decided to not investigate further a potential increase in its element size. As can be observed, the first line in the columns coincides with the most refined mesh case, hence the variation of maximum deformation is zero.
From Table 4.2 it can be observed that two combinations of parameter fulfill the requirement of maximum deformation being below 1%. However, the case with a l_{tip} of 0.1mm was chosen since it features slightly lower number of elements.

4.2.2. CFD Mesh

Being the main focus of the current thesis project the impeller, most of the efforts done in finding a proper numerical grid were done only for this part of the fluid domain assembly. This mesh was generated using ANSYS Turbogrid, a tool made specifically to generated numerical grids for turbomachinery CFD simulations.
In order to find an ”accurate enough” simulation, without falling in too excessive computational times, a mesh convergence study was performed also in this case. In particular, with a fixed y+ of 2 at the walls, the number of elements was varied between 250 000 and 2.5 millions for the rotor, whilst the stator elements were kept constant. Taking the results obtained for the maximum number of elements as most accurate, the mesh with the minimum number of elements but still within 0.1% accuracy was chosen.

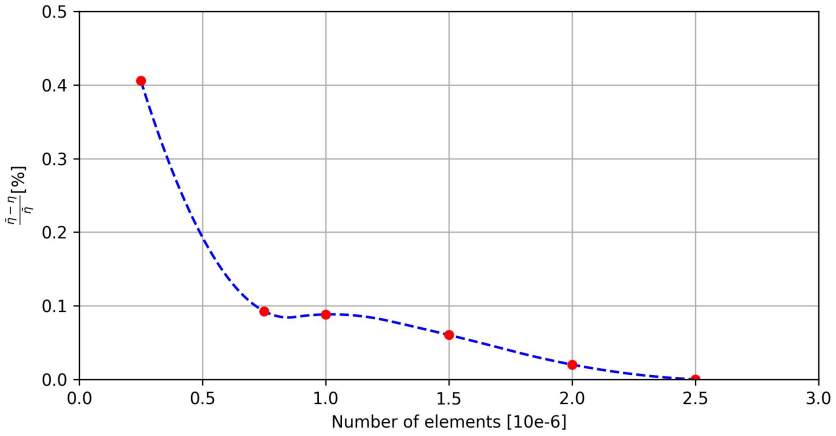

Figure 4.6: Convergence study for the optimization CFD simulations.

As can be observed in Figure 4.6, the mesh with 750 000 elements already respected the accuracy requirement previously stated. However, after visual analysis of such grid, it was decided to use 1 million elements due to the excessive differences in mesh sizes between inlet and wall elements and main flow ones.
Close up pictures of the mesh at the trailing edge and leading edge of the impeller blade are shown respectively in Figure 4.7a and Figure 4.7b, whilst the overall numerical grid for the rotor is presented in Figure 4.8.

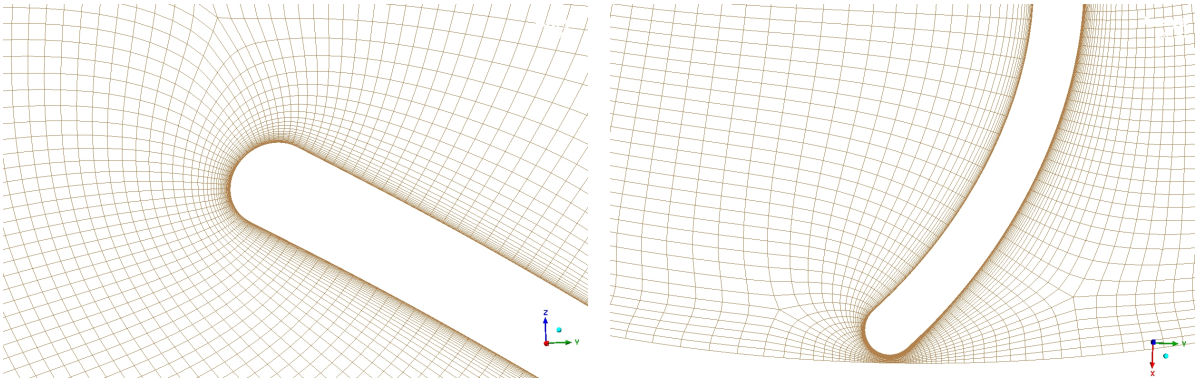

(a) Close up view of the trailing edge mesh of the ORCHID impeller.

(b) Close up view of the leading edge mesh of the ORCHID impeller.

Figure 4.7: Close up view of relevant mesh regions of the ORCHID impeller.

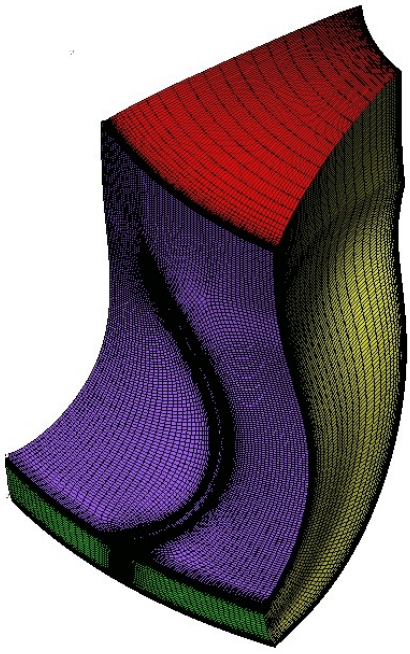

Figure 4.8: Overall mesh of the ORCHID impeller.

On the other hand, the number of elements for the numerical grid of the stator is drastically reduced respect to the one of the impeller. To get accurate results of the stator flow field, and especially capturing the shock waves and the wake effects, a far finer grid would be needed. However, since this is not the focus of this research, and since a slightly inaccurate prediction of the stator flow field is not expected to affect the optimization outcome, it was decided to use around 500 000 elements for this region, with a y+ around 10.
The overall numerical grid for the stator can be found in Figure 4.9:

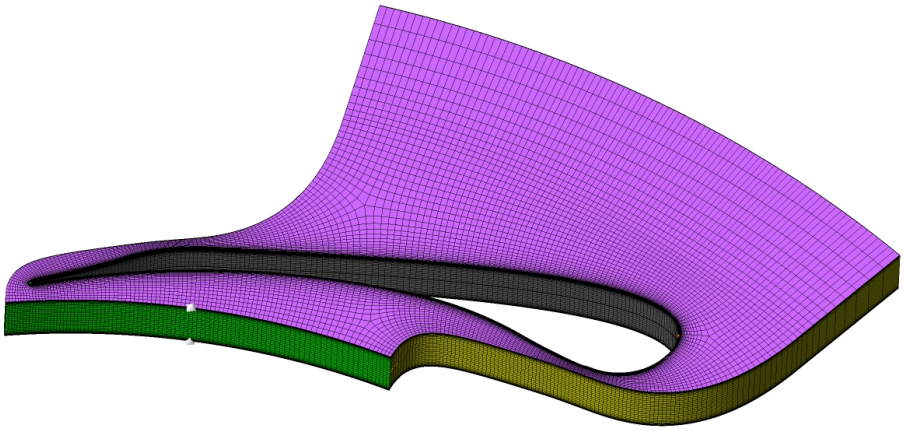

Figure 4.9: Overall mesh of the ORCHID stator.

4.3. FEM Setup

As already mentioned, only static structural FEA simulations have been performed in the optimization framework. They were performed on a blade stand-alone domain, meaning that no hub or other parts of the impeller aside from the blade was included. The software employed is the Static Structural module in Ansys Workbench.
An overview of the boundary conditions employed can be found in Table 4.3:

Table 4.3: FEM simulations boundary conditions.

Rotational velocity	$98119\ rpm$
Thermal condition	$250\ °C$
Fixed support	-
System coupling	-

It is worth specifying that, whilst the first two boundary conditions are applied to the entire part body, the last two are surface conditions. The fixed support and system coupling boundary conditions are then applied to the blade root and to the blade wet surface respectively. In particular, the latter exchanges information with the CFD simulations, receiving data on the pressure load applied on the blade and providing info on the displacements, which are then transferred to the fluid domain as mesh deformation parameter.
To conclude, the large displacement option has been used in order to take into account non-linear effects due to high deformations.

4.4. CFD Setup

To better present the setup used for the CFD simulations, in Figure 4.10 the assembly of the fluid dynamic domain is shown.

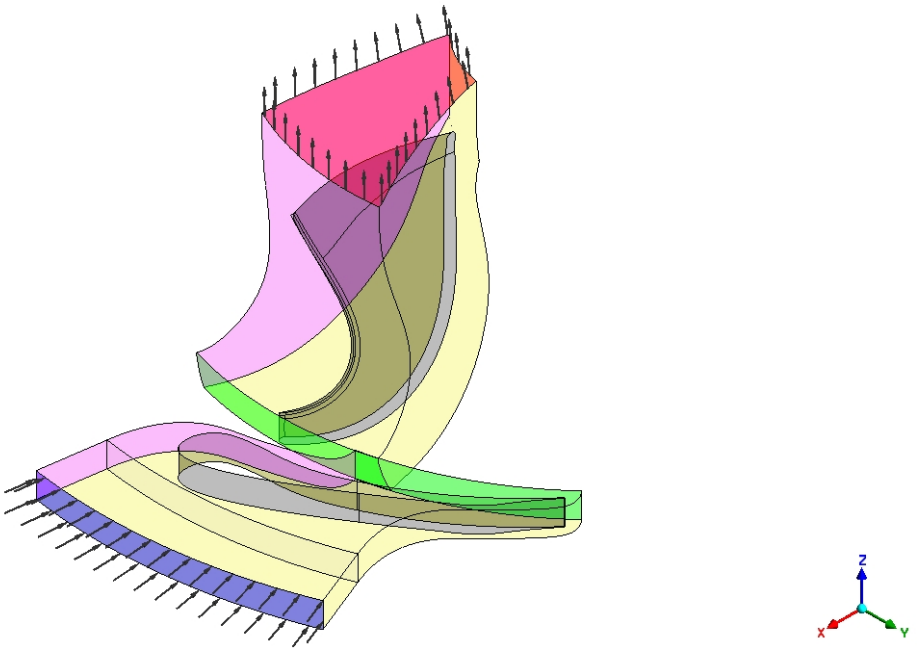

Figure 4.10: Explanatory image for CFD boundary conditions.

where the different boundaries are identified by different colors as follow:

- Inlet: blue
- Outlet: red
- Hub: yellow
- Shroud: transparent for clarity
- Blades: grey
- Periodic interface: pink (only one of the two, the other one is transparent for clarity)
- Mixing plane interface: green

As can be observed from the above picture, only a single stator and rotor blade vane are used to reduce computational time and then rotational periodicity is applied.
The entire domain is divided into two subdomains, rotor and stator. Both of them use the SST turbulence model. The main difference, aside from the geometry, is that while the stator is a stationary domain, the rotor features 98119rpm of rotational speed as domain motion. Moreover, the rotor allows for a deformation of the mesh to account for the coupling with static structural FEA, whilst the stator does not.
The hub, shroud and blade are modelled as simple walls (rotating and stationary ones for rotor and stator respectively) with no slip condition. The remaining boundaries,

inlet, outlet and mixing plane, are described in Table 4.4, Table 4.5 and Table 4.6 respectively for clearness:

Table 4.4: Inlet boundary conditions

Inlet	
Total pressure	$18.093\ bar$
Flow direction	normal to boundary
Turbulence intensity	medium (5%)
Total temperature	$300°C$

Table 4.5: Outlet boundary conditions

Outlet	
Average static pressure	$0.443\ bar$
Pressure averaging	Over the whole outlet

Table 4.6: Mixing plane boundary conditions

Mixing plane	
Pressure profile decay	3%
Implicit pressure averaging	Active
Downstream velocity constraint	Constant total pressure
Pitch angle side 1	$30°$
Pitch angle side 2	$32.7272°$

4.5. Surrogate Based Optimization Setup

In the current section, the setup of the surrogate based optimization is presented, with info regarding the algorithms employed, the number of simulations run and the accuracy of the response surface generated. In particular, in Table 4.7, Table 4.8 and Table 4.9 the main characteristics of the Design of Experiments (DoE), the Surrogate Model (SM) and the Optimization are respectively described.
As already mentioned, the DoE is used to select the initial sample points to be evaluated for the generation of the surrogate model. In this case, an iterative algorithm has been used, with the goal of maximizing the spreadness of the design points. This first step required the simulation of 45 design points:

Table 4.7: Design of Experiment.

Algorithm	Optimal Space Filling
Design type	Max-Min Distance
Maximum number of cycles	15
Number of initial points	45

After the initial sampling method has been set up, the surrogate model was chosen. The Kriging algorithm was employed, and additional 20 refinement points have been added using its automatic refinement capability.
In fact, due to the well-known issues of the OSF algorithm in properly sampling the design space boundaries, and the first unrefined response surfaces generated being not robust enough, the need of several refinement point was identified. After more points were added to the initial response surface (all automatically generated at the borders of the design space) the results changed significantly. Therefore, after a trade between computational time and response surface quality, 20 refinement points were deemed sufficient to cover the design space boundaries and give robustness to the surrogate generated.

Table 4.8: Surrogate Model.

Algorithm	Kriging
Number of refinement points	20
Number of verification points	3

Therefore, a number of 68 FSI (one CFD and one structural FEA) simulations were performed for each case. Considering that every design point evaluation takes around 1 hour, a total of 3 days were needed to perform each optimization.
Finally, the Non-Linear Programming by Quadratic Lagrangian (NLPQL) algorithm was used to find the optimal point. The optimum found using this method closely matched the optimum found when changing the initial guess and when using different optimization algorithms, gradient-based or not, providing confidence towards the good accuracy of the results obtained.

Table 4.9: Optimization of the Surrogate Model.

Algorithm	NLPQL
Initial Finite Difference Delta (%)	0,001
Maximum number of iterations	100

5

Results

In this chapter, the results from the multidisciplinary design optimization performed are presented. Moreover, an in depth analysis on the coupling between the structural and fluid dynamic field is performed and discussed, to aid the explanation and understanding of the optimization results.
The study cases analyzed are hereafter referred to as SC1, SC2 and SC3, whose high-level design features are presented in Table 5.1:

Table 5.1: Nomenclature for the different study cases.

Name	Material	Manufacturing Method
SC1	316 Stainless Steel	CNC
SC2	Ti-6Al-4V	CNC
SC3	316 Stainless Steel	Additive Manufacturing

The chapter is split into two main sections. section 5.1 presents an analysis of the fluid-structure interaction, with the main objective of understanding the impact of the different loads on the structural deformations and how these affect the fluid-dynamic efficiency. In section 5.2 the focus is shifted on the discussion of the results for the three multi-disciplinary optimizations performed.

5.1. Fluid-Structure Interaction Analysis

As mentioned, this section focuses on different analyses performed on the fluid-structure interaction behaviour. In subsection 5.1.1, the different loads acting on the blade and their effect are studied. Also, a case where the deformations have a completely different behaviour compared to the initial design is presented. Finally, sensitivities on the different contributions on deformations due to the different parameters are shown. On the other hand, subsection 5.1.2 presents what are the effects of such deformations on the turbine flowfield.

5.1.1. Deformations Analysis

Conventional radial turbines [34][35] commonly feature radial fibered blading at both the tip and exducer. At the inlet, a radial blade offers good structural performance under the extreme thermal and centrifugal stresses. At the exducer, where the blade height can be 3 to 4 times the leading edge height, radial fiber blades help to prevent off-plane centrifugal load deformations, which can lead to severe consequences. As a result, such impellers are bound to operate at high negative incidence (up to 30° [36]) and minimal exducer rake angle, with a great penalty on their aerodynamics. This is not the case when considering unconventional turbines, such as the high-pressure ratio Organic Rankine Cycle turbine subject of this study. Due to the employment of molecularly complex fluids and the moderate maximum temperatures achieved in ORC cycles, these turbines operate at much lower rotational speeds and experience smaller thermal loads. This translates in more freedom for the designer when it comes to the aerodynamic shapes, including non radial fibered blades at both the inlet and the exducer. Nevertheless, proper understanding of the influence that the structural deformations of these complex shapes have on the aerodynamic performance is key to optimize, and enhance the performance of these devices even further.
To better understand this fluid-structure interaction, the deformation of blades made of different materials and generated with different combinations of the design variables has been analysed and discussed.
It is worth specifying that, although the different designs shown in the following come from the population under investigation in the optimization, the studies presented in this subsection were performed using a 1-way fluid-structure interaction, rather than a 2-way fsi as in the optimization, for sake of briefness. Hence, rather than performing CFD simulations for each of these structural simulations, the results from a fixed fluid dynamic simulation are imported and used for all the structural studies in the following. This introduces a small inaccuracy due to the pressure loads not being changed when changing geometry, but the computational time is drastically reduced and important insights can anyway be gathered.

Off-plane blade deformation mechanisms
In this study, the pressure and centrifugal loads have been applied on the blade simultaneously and separated, in order to distinguish their individual impact on the overall blade deformation. Moreover, only for this analysis another case has been added, where the thickness is reduced as in SC3, but the material used is titanium as in SC2, which will be called SC4. This is done in order to gather additional insights on the structural behaviour of the part. An overview of the deformation results for each study case can be found in the table below:

Table 5.2: Deformations for the initial design points for the different study cases.

Forcing	SC1	SC2	SC3	SC4
All loads [mm]	0.0559	0.0542	0.096071	0.0888
Centrifugal [mm]	0.0624	0.0653	0.11125	0.11275
Pressure [mm]	0.0061	0.0118	0.013619	0.02606

The comparison of the overall deformations for SC1 and SC2 from Table 5.2 is somewhat counter-intuitive. In fact, the Young modulus of stainless steel at 300° is twice as large compared to that of titanium, while the deformations for SC1 are slightly higher than for SC2. However, using the superposition of the effects and considering the two loads acting on the blade independently, one can see that the deformations due to the blade loading and the centrifugal force are opposite in sign. This difference can be appreciated in Figure 5.1:

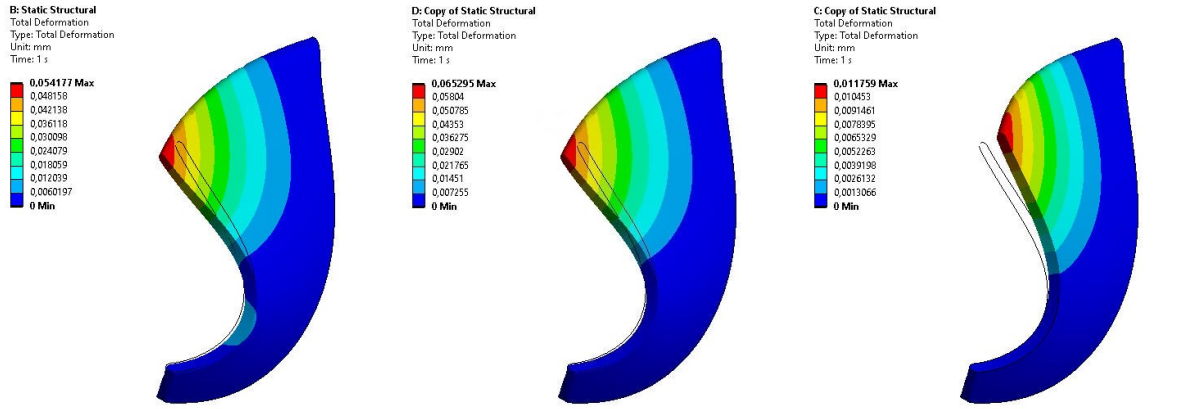

(a) Deformations on the initial geometry for SC2 when both centrifugal and pressure loads are applied.

(b) Deformations on the initial geometry for SC2 when only centrifugal loads are applied.

(c) Deformations on the initial geometry for SC2 when only rotational loads are applied.

Figure 5.1: Deformations on the initial geometry for SC2.

When only the pressure loads are considered, which are surface forces, the stainless steel design SC1 deforms far less than the titanium SC2. In this case, the material's elasticity is the main driver for the structural deformation, since the geometry (and thus the "geometrical stiffness") is the same. However, when looking at the deformation occurred under the action of centrifugal loads, SC1 and SC2 are comparable despite the different material characteristics. Recalling that the centrifugal force is a body force, in this case the density ratio between the two materials also drives the structural behavior under load. In fact, titanium's density is about half that of stainless steel, making the latter experience a higher load at the same rotational speed. Therefore, despite the inherently lower flexibility of stainless steel, SC1 deforms as much as SC2 at the design rotational speed, due to the higher density. As a result, being the deformations due to centrifugal loads almost identical, and the counteracting deformation due to pressure loads higher for titanium, stainless steel experiences higher overall deformation under combined load, as shown.
As expected, the same loads lead to higher deformations in the SC3 case, whose geometry is parameterized considering a 25% reduction in root blade thickness compared to SC1 and SC2. It is interesting to notice that, whilst the pressure load induced deformations are more than twice as high as SC1, the centrifugal force induced deformations don't increase as much. In fact, the decrease in thickness strongly affects the mass of the part, which results in a lower centrifugal force. However, the total deformation increases due to the reduced stiffness of SC3, which makes the blades more prone to deform under the same pressure loads. The same considerations also

apply to SC4, when compared to SC2.
A further reduction of 0.2mm in root blade thickness showed, once again, a more than twofold increase in total blade deformation. As previously corroborated, also in this case pressure load induced deformations become more and more important over the centrifugal load induced ones. Though, these results have not been reported here because not strictly relevant with the study at hand, as a further reduction in blade thickness could lead to increasingly more challenging manufacturing and is therefore not considered in this study.
Finally, it is important to stress that the described trade-off between stiffness and mass is strictly dependent on the geometry, thus the blade shape. As an example, radial fiber blades will tend to show more sensitivity to deformations induced by pressure loads, while non radial fiber blades such as in the current impeller will show sensitivity to both contributions.

An analysis on completely different deformation behaviours is shown here for the same material and thicknesses but different design points.
Once the design space has been investigated during the optimizations by means of fluid-structure interaction simulations, some of the design points where high deformation occurred have been further analysed. Important differences were noticed and a comparison between the maximum deformation point and the initial design point has been done. In particular, from Figure 5.2 it can be noticed that the total deformations the two shapes undergo are completely different. In fact, in the initial design the blade tends to ”twist” still more compared to the underformed shape, flattening and getting the leading edge tip closer to the hub, Figure 5.2a. On the other hand, in Figure 5.2b it can be seen that the blade ”untwists”, becoming more radial instead.

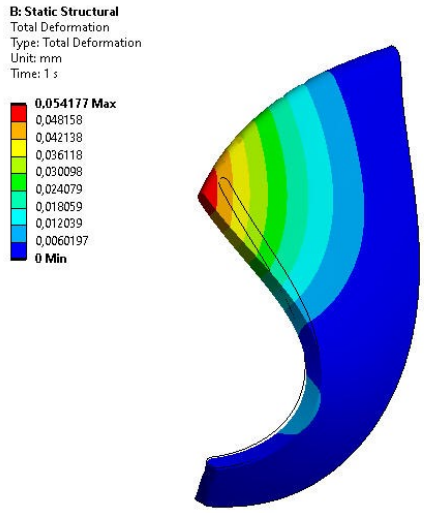

(a) Deformations behaviour on the initial geometry when all loads are considered for SC2.

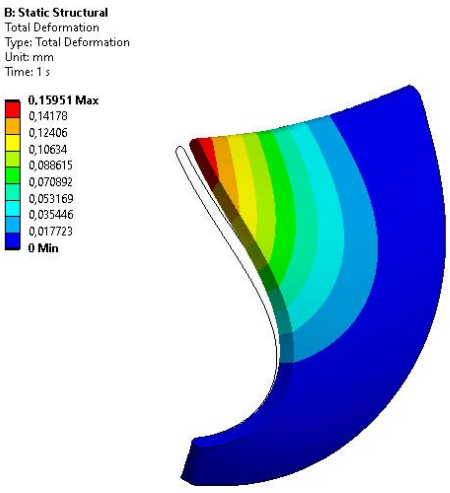

(b) Deformations behaviour on on the maximum deformation geometry when all loads are considered for SC2.

Figure 5.2: Comparison between two design points with opposite deformation behaviour when all loads are considered for SC2.

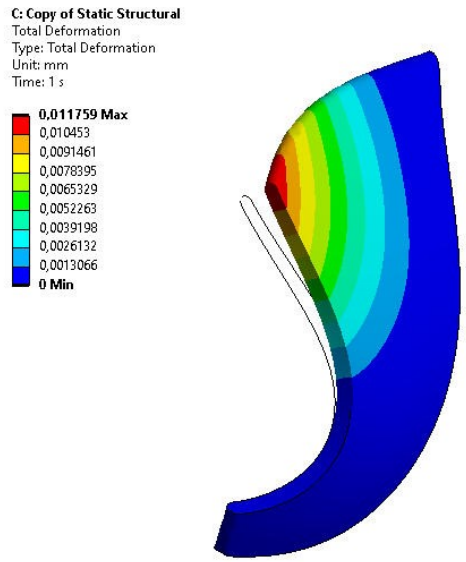

(a) Deformations behaviour on the initial geometry when only pressure loads are considered for SC2.

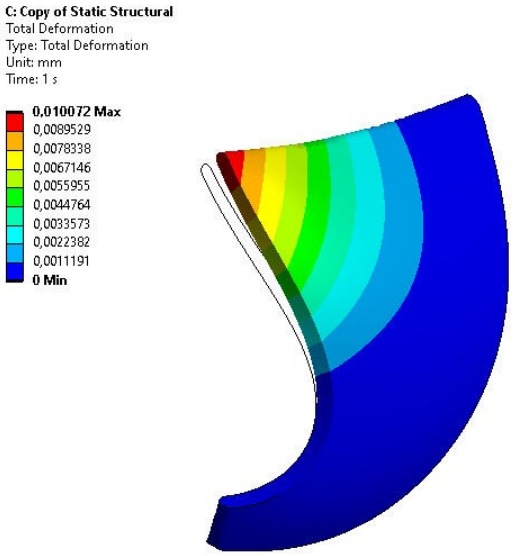

(b) Deformations behaviour on the maximum deformation geometry when only pressure loads are considered for SC2.

Figure 5.3: Comparison between two design points with opposite deformation behaviour when only pressure loads are considered for SC2.

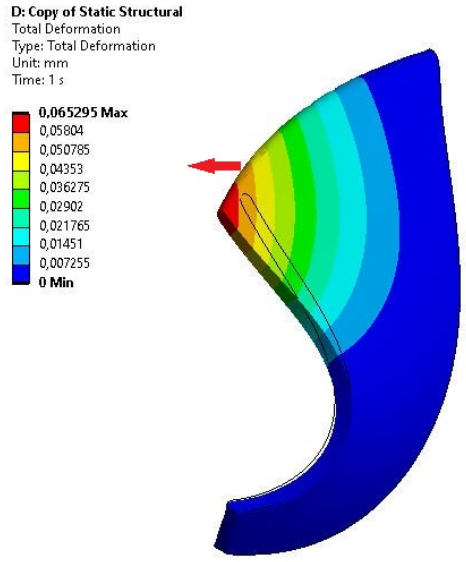

(a) Deformations behaviour on the initial geometry when only centrifugal loads are considered for SC2.

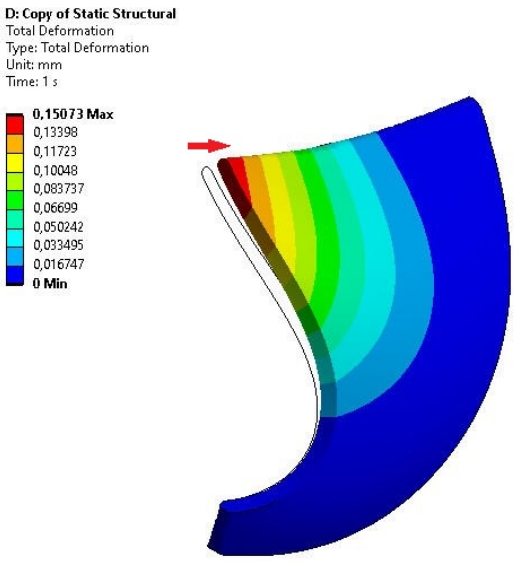

(b) Deformations behaviour on on the maximum deformation geometry when only centrifugal loads are considered for SC2.

Figure 5.4: Comparison between two design points with opposite deformation behaviour when only centrifugal loads are considered for SC2.

To investigate the reason at the base of such difference, the deformations due to pressure and centrifugal loads have been studied independently from each other also for the maximum deformation point. Whilst the pressure load deformations, shown in Figure 5.3, follow the same direction, due to the pressure applied being the same, the main difference can be noticed when the centrifugal loads are looked at. In Figure 5.4 it is shown that the difference between the two deformations due to rotation are in the order of $0.2mm$ with the direction of deformations (indicated from the small red arrows) being opposite, which is quite high considering that the blade tip is only $0.6mm$ for these cases. When SC3 is considered, this difference is still higher due to the thinner blade leading to higher geometry variations. In the following it will be shown how the different design variables affect the maximum deformation.
This is particularly interesting considering that the deformation of the blade deforms the position and the area of the throat in the blade-to-blade channel. Therefore, it is expected that a blade deforming as in Figure 5.2b will have a larger minimum throat area, and hence a slower flow at the exducer. On the other hand, for designs featuring a deformation in the opposite direction as in Figure 5.2a the opposite is expected. This directly affects the turbine performances, in particular when considering the total-to-static, rather than total-to-total efficiency.

Effect of design variables on blade deformation
To better understand how the deformations vary in the design space, a parametric study has been performed on the blade. In particular, the parametric correlation tool in Ansys has been used for this. This creates a design of experiments similarly on how is done for the response surface optimization and perform a correlation evaluation with the results obtained. For each of these studies, 200 design points have been used (and FEA simulations evaluated) and a Spearman's Rank Correlation has been used to create correlation coefficients [27]. The design space used for such analyses is slightly different from the optimization's one, the different variables can be seen in :

Table 5.3: Educate range of design variables used in the optimization.

Design variables	x_{low}	x_i	x_{up}
β_1	$37°$	$45°$	$53°$
β_4	$-65.2°$	$-57.2°$	$-49.2°$
$\beta_{2,hub}$	$-29.4°$	$-9.4°$	$10.6°$
$\beta_{3,hub}$	$-66.8°$	$-46.8°$	$-26.8°$
$\beta_{2,tip}$	$5.4°$	$25.4°$	$45.4°$
$\beta_{3,tip}$	$-106.1°$	$-86.1°$	$-66.1°$

The main reason why the design space has been adapted is that for the parameter correlation the impact of an input on the output is driven by two different factors: how much the output changes across the input range, and the width of the range itself given to the inputs. Therefore, it was decided to get the design space "as uniform as possible" to have a more immediate understanding of the sensitivity studies performed.

This was done by defining an identical range between the first two design points (β_1 and β_4), and the same was done for the remaining variables.
The results for the different sensitivity analyses performed are presented in Figure 5.5:

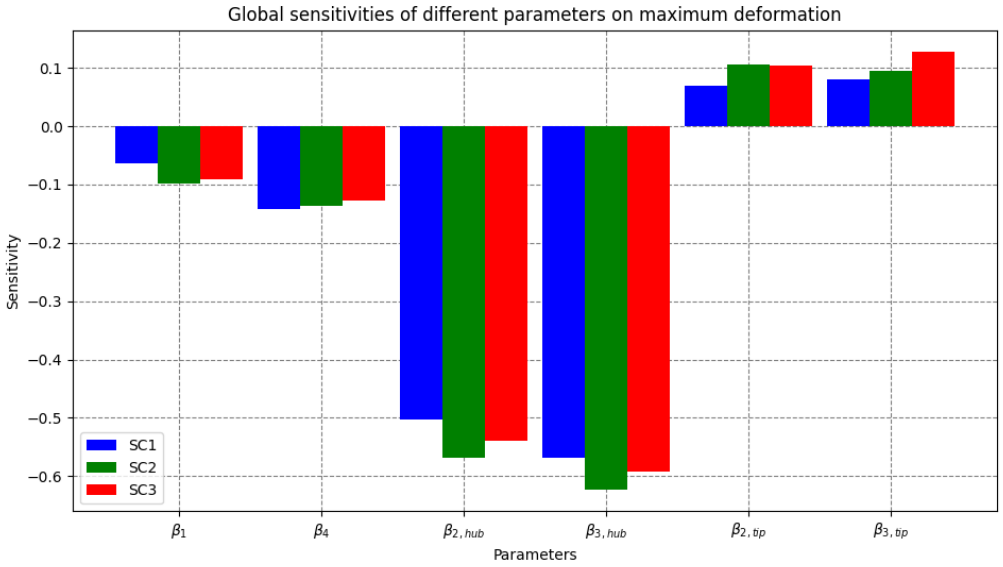

Figure 5.5: Sensitivity analysis of the influence of the different optimization parameters on the blade maximum deformation for the different study cases.

The diagram presents the influence of the different parameters on the maximum deformation of the blade. In particular, they are calculated considering how much is the variation of the output over the range of the parameter, normalized over the output range. Moreover, let's not forget that the sensitivity of the first two parameters, β_1 and β_4, should be seen independently from the others since the input range is far smaller, 16 degrees rather than 40 as for the others.
From the diagram, it can be observed that the Bezier points at the hub have a stronger influence over the deformations compared to the ones at the tip. Moreover, the sensitivity reveals an inverse trend for them. Therefore, when the parameters $\beta_{2,hub}$ and $\beta_{3,hub}$ are increased the deformations tend to reduce, whilst for $\beta_{2,tip}$ and $\beta_{3,tip}$ the opposite can be said. Regarding the higher influence of the parameters at hub, this can be explained considering first of all that the mass of the lower part of the blade is higher than the other half, due to the linearly decreasing thickness over the span. Moreover, it is logical that a higher load on the lower part of the blade will cause a more pronounced deformation in that region, which will have strong effects on the geometry of the tip as well. However, the opposite can't be said for the parameters at tip.
Speaking of the direction of the sensitivity, a precise explanation is not easy to find, because every parameter affects the shape of the entire blade. For instance, the point at the station 3 highly affects the shape of the trailing edge. Moreover, the curvature at the hub and the one at the tip strongly influence the "flatness" of the blade. Generally speaking, it has been seen that an increase of the quantities at the hub tends to move the blade, or the span lines, in a way that it is more aligned to the radial direction, presumably decreasing the centrifugal loads. On the other hand, when the quantities at

the hub are decreased, the blade starts deforming becoming spanwise less ”straight”, which leads to a longer distance from hub to tip and hence higher tip deformations. Regarding the angles at inlet and outlet, it can be observed from Figure 5.5 that the outlet has a higher effect on deformations. Although the inlet is more distant from the axis of rotation, this was expected due to the far longer span of the trailing edge compared to the leading edge. In this case the inverse sensitivity trend observed for the inlet is mainly due to the blade flattening when β_1 is decreased. On the other hand, when β_4 is decreased the trailing edge shape move further away from the radial line, and due to the high span this factor prevails over the general change of blade overhang angle.
All in all, it has been tried to give a reasoning to the trends shown in Figure 5.5. However, the high non-linearity of the structural behaviour for this part and the opposite deformation behaviour shown in the previous paragraph makes almost impossible to define a clear and exact reason behind every parameter's sensitivity. This further shows how the deformation behaviour is highly unpredictable for this design, and can't be assumed without further analysis.

In order to better understand the actual difference in sensitivities between all the parameters, an additional parametric study has been performed on SC1 with all variables having the same range ($20°$). This can be observed in Figure 5.6:

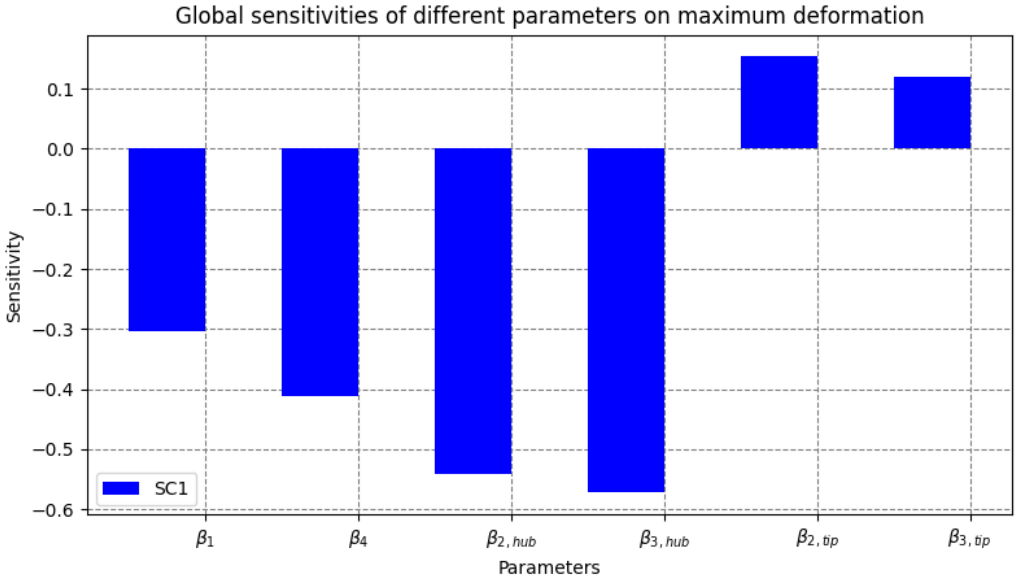

Figure 5.6: Sensitivity analysis of the influence of the different optimization parameters on the blade maximum deformation for SC1 with uniform design space.

From the diagram above it is evident that the main trend is unchanged, but differently from before, the influence of the inlet and outlet angles is drastically increased now, which makes sense considering the radially outward position of β_1 and the long span of β_4. This influence keeps being lower than the hub Bezier points, but this is probably explained by the inlet and outlet angle being parameterized as spanwise constant.

5.1.2. Flow-Field behaviour due to Deformations

In order to investigate the influence of structural deformation on fluid dynamic efficiency, a comparison between the undeformed and deformed designs should be carried out. Though, to make sure the comparison at different materials and blade thickness is fair, an impeller characterized by the same design variables should be used. When looking at the whole population of the three different MDOs performed, the maximum deformation design was especially interesting. In fact, it was found that the combination of design variables leading to maximum deformation was the same for the SC1, SC2 and SC3 test case. Thus, this specific design point represents a good candidate for further investigation.
In Table 5.4 the total-to-static efficiencies obtained from 2nd order accurate CFD simulations on the cold and hot design of the three cases are presented. In particular, high resolution schemes were used for both the calculation of conservative fluxes and turbulence closure for this analysis, differently from what was done in the optimizations. In addition, the same computational grids previously introduced were used and a computation effort of about 1000 iterations was ensured to obtain properly converged solutions.
From now on the cases with structural transformation (hence the hot design) are referred to with an asterisk used as apex, to better clarify the difference between undeformed and deformed parameters and results. As an example, case SC1 is the undeformed case with stainless steel and assuming CNC manufacturing design features and constraints, and SC1* is the corresponding deformed case.

Table 5.4: Deformations and total-to-static efficiencies for the design points with maximum deformation in the design space for the different study cases.

	SC1	**SC2**	**SC3**
Deformation [mm]	0.308	0.153	0.461
Efficiency [%]	81.259	81.259	81.747
Efficiency* [%]	81.903	81.538	82.313
Efficiency variation [%]	0.79	0.34	0.69

From the table above, it can be noticed that the stainless steel case SC1 showcases a larger total deformation than the titanium case SC2. This trend is opposite compared to what was shown in Table 5.2. This is likely due to a change in centrifugal loads compared to the initial design, which made the density of the part being a more important factor compared to the Young modulus in deformation behaviour in this case.
From Table 5.4 one can also infer that higher deformations lead to increased fluid-dynamic efficiency for this design point. However, it needs to be stressed that this relation can not be generalized over the design space, since the combinations of the design parameters are ever different, and the behaviour of the structural changes are significantly different.
Nevertheless, one can can draw some conclusions related to the effect of deformation on this specific design point, which is relevant in terms of understanding the physical

mechanisms at play. While the undeformed cases (SC1 and SC2) don't differ in fluid-dynamic performance, as they are the exact same geometry, things become more interesting when including the the structural deformation (SC1* and SC2*). In fact, about 0.8% increase in efficiency occurs between the initial undeformed impeller and the deformed case. The current method generated a cloud of 68 unique designs within less than 4% range of efficiency variation. Part of this variation is obviously due to the influence of the design variables on the objective function (the efficiency), as if there was no structural deformation and we were purely looking at the impact of changes in blade shape on performance. On the other hand, part of such variation can be attributed to the inclusion in the model of a structural deformation, which would otherwise have to be considered using trial and error, until all constraints are satisfied. In particular, if a fluid dynamic optimization was performed without considering deformations, and the optimum was found in the design area characterised by high deformations, we can conclude that the efficiencies for the optimum design found would greatly differ from the actual performances. This corroborates with the fact that a multi-disciplinary optimization strategy has the potential to greatly improve the performance of a given design, while ensuring manufacturability and structural resistance, and possibly reduce the design iterations, and hence the computational effort.
To better understand why these performance gap, a more detailed look at the fluid dynamic behaviour for the deformed and undeformed cases is necessary. In Figure 5.7, the normalized entropy contours with respect to the stator inlet at different values of meridional length are shown for the two cases. One can notice from the middle contour that the entropy generation for the SC1 case reaches the maximum on a wider region of the flow. Flow recirculation in that region is something often found in radial inlet turbines and it is caused by the adverse pressure gradient due to the camberline curvature. This vortical structure is then "pushed" radially toward the shroud due to the meridional channel shape and the Coriolis force. The contours below suggests that the flow recirculation of the undeformed case leads to higher entropy generation within the bladed passage.

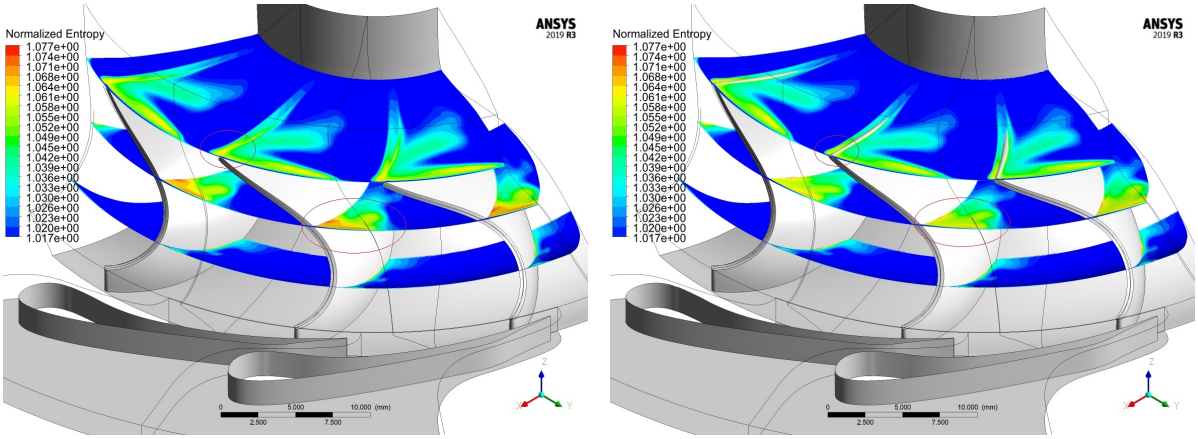

(a) Contours of normalized entropy at different meridional locations for the cold design of the maximum deformation point of SC1.

(b) Contours of normalized entropy at different meridional locations for the hot design of the maximum deformation point of SC1.

Figure 5.7: Contours of normalized entropy at different meridional locations for the hot and the cold design of the maximum deformation point of SC1.

Moreover, if taking a closer look at the tip of the trailing edge, it is visible a small region where entropy is higher for Figure 5.7a rather than in Figure 5.7b. As mentioned previously, this deformation behaviour tends to move the blade radially, in a mechanism of ”untwisting”. This results in an increase of area of the blade throat, particularly at the tip where the most deformations occur, which might lead to slightly higher velocities for the cold design compared to the hot one.

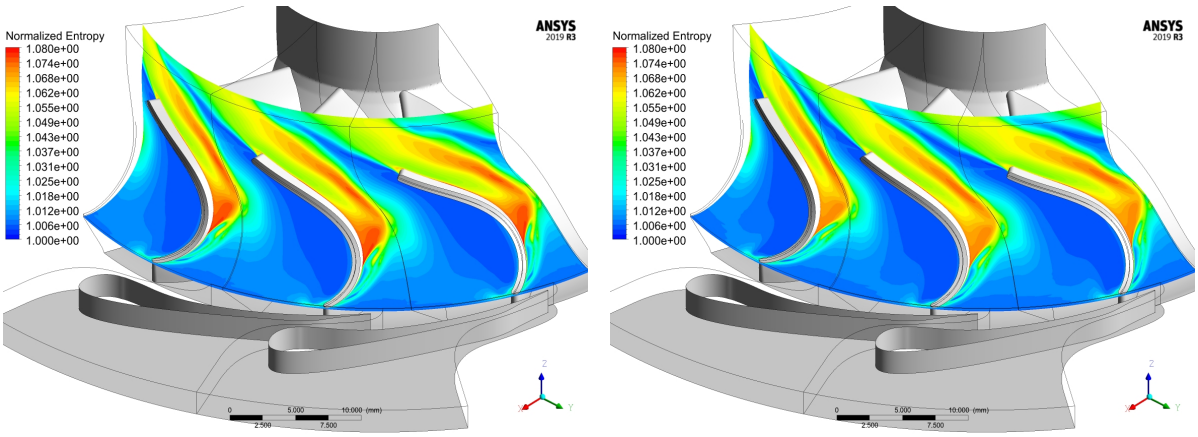

(a) Streamlines visualization for the cold design for the maximum deformation point of SC1.

(b) Streamlines visualization for the hot design for the maximum deformation point of SC1.

Figure 5.8: Streamlines visualization for the cold and the hot design for the maximum deformation point of SC1.

In Figure 5.8, the contours at high constant span are shown to better inspect this behaviour in correspondence to where the maximum deformation takes place. From these, it is visible how the entropy generation due to flow recirculation in the undeformed geometry is higher, although present in both cases.
Another important consequence of deformation is represented by the area variation in the shroud clearance gap. In fact, when structural deformations are accounted for, the shroud clearance gap distribution is subject to local changes along the streamwise direction. Therefore, one can expect different tip gap mass flows and therefore an impact on the stage performance. By calculating the tip gap mass flow rate for the cold and hot blades, it was found that up to 2.35% decrease in tip gap flow rate is achieved in the latter. When considering solely the region of gap corresponding to high deformations of the blade, hence the exducer portion which is mainly axial shown in Figure 5.9, the leakage further increases to 5.29%, along with a decrease in the tip gap passage area of around 3%.

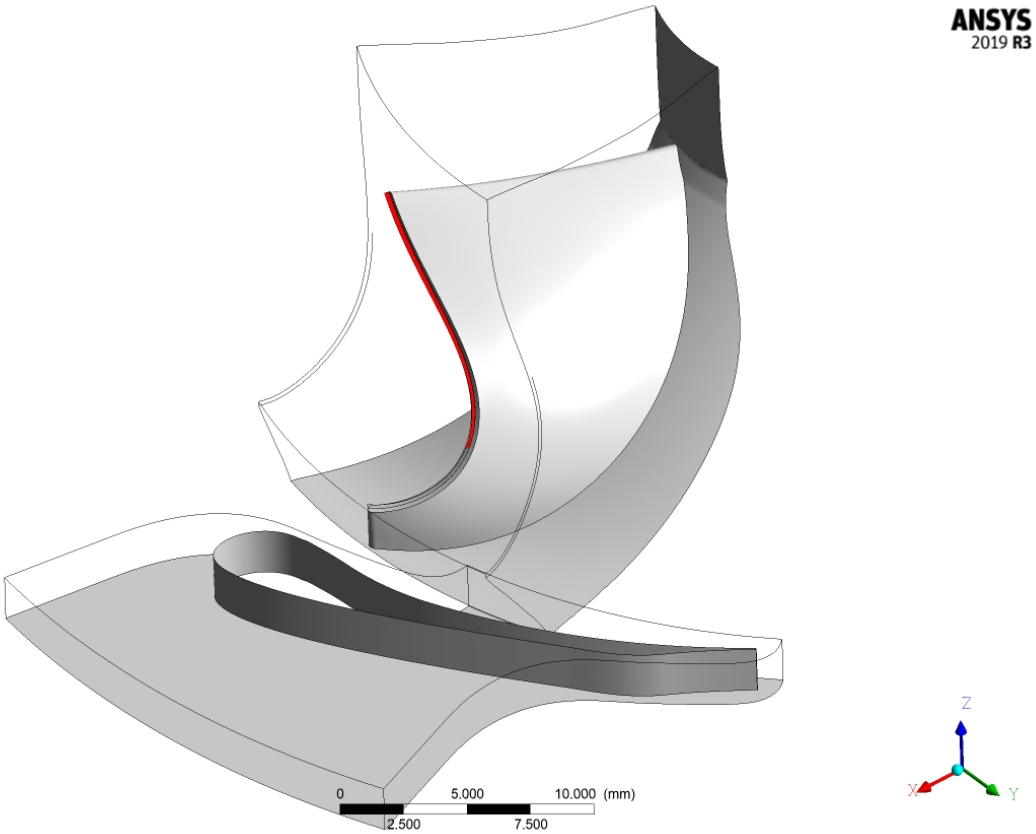

Figure 5.9: Figure showing portion of tip gap used to calculate tip leakage between pressure and suction side.

To investigate the difference due to the tip leakage of the blade, simulations without tip gap have been performed. In Table 5.5 the values for the different simulations are shown for comparison:

Table 5.5: Performances of SC1 and SC1* with and without tip gap for the design point with maximum deformation.

Efficiency	**SC1**	**SC1***
With Tip [%]	81.259	81.903
Without Tip [%]	84.822	85.407

As expected, the efficiency is greatly increased when no tip gap is considered. However, the influence of the tip leakage on the efficiency between SC1 and SC1* is not as high as expected. In fact, it can be observed that the efficiency gap was around 0.65% for the case with gap, whilst it is reduced to 0.58% when not considering it. This shows that most of the efficiency difference is mainly due to the deformation of the blade channel itself, and hence to recirculation reduction in the channel, rather than the change in tip gap mass flow.

5.2. Optimization Results

This second part of the chapter focuses on the results of the multidisciplinary optimizations performed, with particular focus on the performances, and hence the fluid dynamic side of the fsi.
Generally speaking, it was observed that the each design point for the fluid-structure interaction evaluation took around one hour to evaluate. On the other hand, the same setup with same number of overall iterations has been run with only CFD simulations, and a reduction of computational time to 45 minutes for each design point has been observed. This is not a negligible amount of time, which is not directly coming from the structural simulations itself (the small amount of elements results in a FEM computational time of less than 5 minutes). The additional time is probably due to the initialization of the CFD and FEM simulations in the system coupling and the transfer of data between the two at every coupling iteration. However, the ratio of duration between the multidisciplinary and the fluid dynamic only simulations can't be directly applied to every other case. In fact, it is not known how this number scale when scaling the element number of the two numerical grids, and if the mesh used for the CFD simulations was incresed, most probably the difference would be reduced. On the other hand, it has been noticed that an increased number of fsi iterations would results in slightly more accurate results, particularly regarding the data transfer of part deformation to fluid dynamic mesh displacement. An increase in the number of coupling iterations would substantially increase computational time, since the CFD simulations need to find a stable solution for every data transfer step.
Moreover, one of the main difficulties in the implementation of the framework has been the occurring of errors due to generation of negative volume elements in the CFD numerical grid due to the mesh displacement produced by the blade deformations. This is particularly due to the very small element side in correspondence of the blade, which is where the deformations occur. Therefore, in particular for SC3, where the blade is thinner and the deformations are higher, several design points in the design of experiments failed to simulate and were replaced with others. This in turn results in a not perfectly uniform distribution of design points. These topics will be mentioned during the subsequent result analysis, and will be better listed in chapter 6, together with possible solutions for future developments.

This subsection is mainly divided in three different parts. The first one, subsection 5.2.1, presents the main numbers resulting from the optimizations for the different study cases and the trade-off performed between them. Next, in subsection 5.2.2 the accuracy of the optimization framework resulting from the trade-off is studied. Finally, in subsection 5.2.3 a detailed flowfield analysis is performed on the optimal design found.

5.2.1. Main Optimization Results and Study Case Trade-off

In this section, the overall results of the optimizations are presented and commented on. Subsequently, the advantages and disadvantages of the different study cases for the ORCHID application are described and a trade-off is drawn. The results of the

study case that is deemed more appropriate for the current application will be then analysed and investigated in more details in subsequent sections.

General Results

The main results of the multidisciplinary optimization performed on the differen manufacturing methods and materials are presented in Table 5.6

Table 5.6: Total-to-static efficiencies of the different study cases at the initial design and optimum design for both cases with and without structural transformation.

	SC1	SC2	SC3
Initial [%]	81.239	81.239	81.785
Initial* [%]	81.217	81.219	81.745
Optimum [%]	82.326	82.286	82.424
Optimum* [%]	82.343	82.313	82.440

As already noticed previously, we can observe that the cold design of the initial guess have same efficiency for SC1 and SC2, whilst SC3 have a higher efficiency. This is due to the design point being the same and SC3 having lower thickness. Interestingly enough, we can observe a design point where the efficiencies are actually reduced when in the hot configuration compared to the cold one. In fact, if looking at the initial guess, the efficiency in all study cases is slightly reduced when the blade deformation is evaluated. The variation is quite small, mainly due to the blade deformations being quite limited for both the initial and the optimum points (few thousandths of a millimeter). This is particularly interesting because the uncertainty in a normal fluid dynamic optimization due to the high variations of efficiency shown in subsection 5.1.2 is still increased if one thinks that a geometry might have positive or negative performance differences between hot and cold design.

When looking at the optimum design points in Table 5.6, the optimum cold design have in this case different efficiencies for the different study cases since the optimal design points are different. The efficiency variation is also in this case quite small, less than half percentage point. As expected for such an optimization, the efficiency of the hot design is in this case higher than for the cold geometry. One would expect SC1 and SC2 to have a final optimum efficiency for the hot design, although different efficiencies for the cold designs make sense. This is due to the geometry being the same, but with a different material. In fact, it would make sense that the optimization found different cold designs that lead to the same shape once the part is deformed, being it the maximum efficiency geometry of the design space. This small difference is probably due to little inaccuracies in the optimization process, that are probably found in the coupling, due to the small amount of iterations set to reduce computational time. Also, the response surface generation algorithm might introduce some inaccuracies. However, this variation of efficiency is very small, in the order of 0.03% in absolute value, hence it doesn't pose important doubts on the optimization accuracy.

Trade-off

When looking at the efficiencies shown in Table 5.6, it is obvious that the differences between different study cases are quite limited. In particular, only a small improvement is seen for the case of additive manufacturing. Due to the variation being quite small, and most of the pros and cons on the different manufacturing methods and materials being mainly considerations, rather than actual numbers, the trade-off to choose the best study case for the ORCHID application will be mainly qualitative, rather than quantitative.

Below, a list of the different driving factors for the decision, together with considerations for the different study cases studied:

- ***Efficiency:*** As already shown and described in Table 5.6, in terms of the performances, SC3 results the best option due to a higher total-to-static efficiency. However, this factor is not considered particularly important for two main reasons. The former being the very small difference compared to the other study cases using CNC. The latter being the objective of the studied part. In fact, the turbine under development is mainly for testing purposes, and not for power generation or propulsion applications. Therefore, the efficiency itself hasn't such a priority role in this case, although still worth to be considered.
- ***Lead Time:*** Although many manufacturer are present in Europe or in the Netherlands for additive manufacturing production, such a complex shaped and thin bladed part is not within the reach of any production provider. Many manufacturer's website states wall thicknesses quite higher than what is set for SC3, hence it will be assumed that the manufacturer is the one who produced the prototype in the first place, the one described in subsection 3.3.1.
  When considering lead time for the part, the CNC cases have strong advantages. First of all, the CNC manufacturer is located in the TU Delft campus, making any lead time for delivery needless. Moreover, CNC manufacturing generally features sufficient surface finishing quality, which makes the part ready to be operated as soon as produced. On the other hand, 3D printing is known for its bad surface finishing, and need for post-processing, such heat treatment to mention one. This makes the production time quite longer if also considering any post production treatment and surface polishing.
- ***Cost:*** Regarding costs, there are quite some uncertainties, since a detailed market research has not been performed. Hence, the quotation received from the 2 manufacturers consulted will be taken. In this regard, an evident "winner" is not so easy to find. In fact, additive manufacturing is mainly quoted based on manufacturing time, and due to the part being so small the costs associated with it results smaller than the quotation received from the CNC provider. On the other hand, considering again the probable need for post-processing and surface finishing (without considering delivery costs if a manufacturer is found in other countries), it will be assumed that the costs for CNC and 3D printing even out completely. However, a difference here can be said between SC1 and SC2. In fact, being generally stainless steel a cheaper, easier to machine material, the cost of it instead of titanium should be lower.
- ***Procurement Easiness:*** In terms of procurement easiness, CNC cases have the great advantage of being manufactured by a provider located inside the TU

Delft campus. This makes any communications far easier, since it is possible to just ”walk in” and speak with the manufacturer. Moreover, the possible avoidance of required post-processing and surface finishing treatments results in the communication to only one provider, rather than having to deal with different possible stakeholders.

Needless to say that there are several other factors that might have a weight in the decision of the manufacturing method and material used, as the common not precise predictability of material properties for additive manufactured parts, thermal and mechanical stresses arising from manufacturing or aeroelasticity differences resulting from the different mass of the materials chosen. However, since further studies would be required to account for these, they will be disregarded for now and the trade-off will only be based on the above listed considerations.
From what has been explained, the only advantage of additive manufacturing for this design is the efficiency gain. However, due to it being quite limited, and the other factors leaning towards CNC manufacturing, the latter is chosen. Moreover, considering the materials, stainless steel is selected, mainly due to the lower cost, manufacturing easiness and higher experience of the manufacturer with such material.
To conclude, if further studies would reveal a higher instability due to higher part density when choosing stainless, the best option might shift to titanium. Moreover, the decision is strongly influenced by the assumption of additive manufacturing needing post-processing and surface finishing, differently from CNC milling. If this might be found to not be the case, the decision on manufacturing method might also be reconsidered.

5.2.2. Optimization Accuracy

In this part of the chapter the accuracy of the optimization study is investigated for SC1, winner of the previous trade-off. In particular, considerations on the system coupling are drawn and remarks on the goodness of fit for the response surface are presented.

System Coupling Convergence
Regarding the accuracy of the system coupling, some information need to be taken into account. As specified previously, a limited number of coupling iterations have been run, only 3. This means that the data transfer between CFD and FEM simulations only take place few times. Although a root mean square (RMS) convergence target of 0.01 was set, this was often not satisfied by the low amount of coupling iterations performed. However, investigating the results of the optimization, it was noticed that the maximum RMS change was found in the maximum deformation design point (lower deformation points have not been investigated since the change in RMS has less influence on the efficiency variation between cold and hot design). In Figure 5.10, the convergence plot for this point is shown:

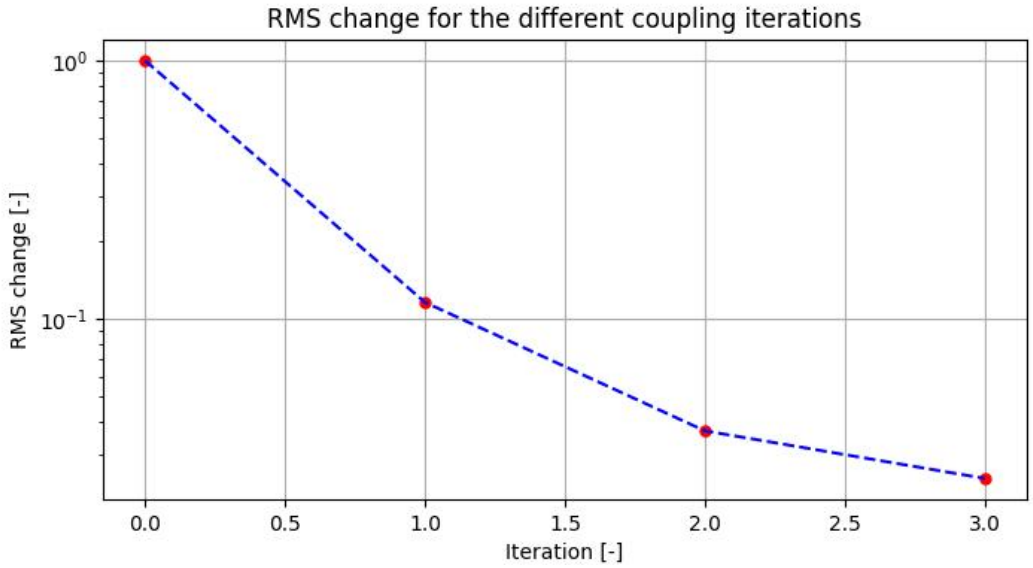

Figure 5.10: RMS change for the maximum deformation design point in SC1.

As can be observed, the target of 0.01 is not reached but the solution is quite close to it, arriving to a RMS change of only 0.024. To make it clearer, this is the difference between the maximum deformation of the structural simulation and the maximum mesh displacement of the CFD simulation. Therefore, considering that this holds for the maximum deformation point, and being it also the one with maximum coupling inaccuracy, the error found is in the order of a hundredth of a milliliter, which is deemed acceptable. Other design points in the design space have both lower deformation and lower RMS change, hence it can be stated that this is the maximum inaccuracy found over the design space for this study case.
It is worth specifying that for the case of SC3, where the blade is thinner and the deformations are higher, it is expected that this value might be slightly higher. However, not relevant error were noticed also in that study case.

Response Surface Accuracy
As far as the response surface accuracy concerns, this is calculated using verification points. In particular, for each optimization the verification points employed are 3. Based on these three points, Ansys calculates what is called the Goodness of Fit of the response surface, by checking the offset of these verification points from the values predicted by the surrogate model generated. For SC1, the goodness of fit is presented in Figure 5.11. In the image, the red squares are the design points evaluated to generate the response surface, whilst the light red dot are the verification points.

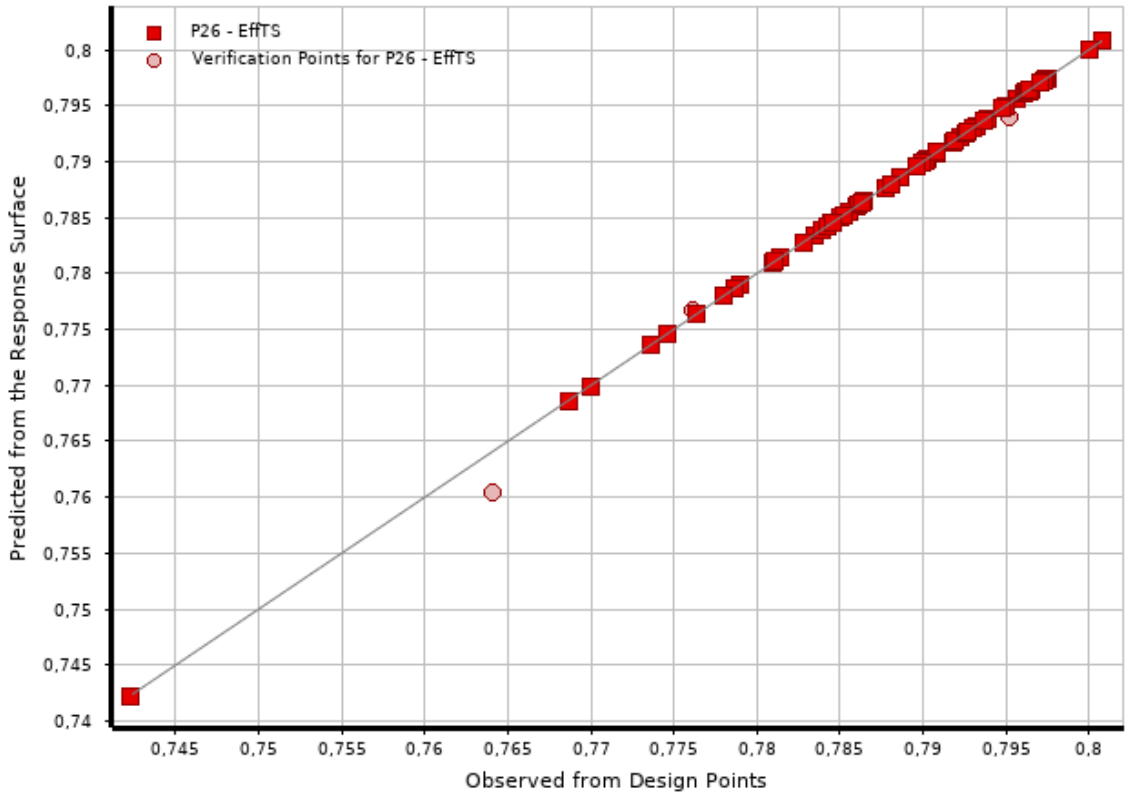

Figure 5.11: Goodness of fit chart for the response surface.

The RMS error calculated for the response surface generated is around 0.3%, which is quite low. On the other hand, when looking at the relative average maximum error, this is around 19%. However, by excluding the most offset verification point (the one with around 76.3% efficiency shown), the relative average absolute error becomes lower than 0.1 efficiency points, which is deemed acceptable. This is mentioned due to this verification point being quite far apart from the other 65 design points evaluated. Another design point also results far off the range of efficiencies evaluated during the optimization. Therefore, it is believed that the results for these two points doesn't come from a physical behaviour of the flow, but from numerical errors.
If we exclude those two points for the reasoning just explained, the accuracy of the response surface results sufficient. Moreover, the optimal points obtained from the optimization have been simulated for further analysis, and the efficiency found by the surrogate model was found to be accurate.

5.2.3. Detailed Flowfield Analysis

Once the study case to be used for the manufacturing of the ORCHID turbine has been selected and the accuracy of the surrogate model investigated, it is interesting to see the reasons why the optimal design found has the highest total-to-static efficiency in the selected design space. In order to do so, the optimal design is studied in comparison with the initial guess. In Table 5.7, the design variables for the optimum are presented together with the initial design values for comparison:

Table 5.7: Initial and optimum design points parameters.

Design Point	β_1	β_4	$\beta_{2,hub}$	$\beta_{3,hub}$	$\beta_{2,tip}$	$\beta_{3,tip}$
Initial	$45°$	$-57.2°$	$-9.4°$	$-46.8°$	$25.4°$	$-86.1°$
Optimum	$37°$	$-55.26°$	$1.53°$	$-31.82°$	$13.73°$	$-82.35°$

An important takeover from the table above is the strong difference in relative inlet angle. In fact, although the other parameters were expected to be relatively away from the initial guess, due to the many changes applied to the previously found optimal design, it was expected for the inlet and the outlet not to change substantially, which is the case for β_4 for example. Moreover, while investigating the local sensitivities of the design variables on the efficiency from the response surface, it was surprisingly noticed that the inlet angle doesn't have a strong influence on efficiency for many design variables combinations investigated. In most of the cases, a change of inlet angle throughout the studied range when the other parameters are fixed, leads to a change in total-to-static efficiency of few decimal points in percentage. The explanation given to this finding is that almost absent clearance between the stator and the rotor, and particularly between mixing plane and rotor leading edge. What is found instead, is that throughout the design space, the driven parameters for efficiency changes are the angles in the second half of the blade from a meridional point of view, therefore $\beta_{3,hub}$, $\beta_{3,tip}$ and β_4.

Since for the maximum deformation point already analyzed, it was noticed that a strong difference in terms of tip leakage was present, the same analysis has been done for this case. When looking at the total tip leakage mass flow between the two different designs, it is calculated that the optimal design features a mass flow over the tip around 8.42% lower compared to the initial design with a difference in tip area in the order of 4%. On the other hand, when only looking at the part of the blade toward the excducer, the one visible in Figure 5.9, this tip leakage difference increases, it being around 14.4%. Below, in Table 5.8 the efficiencies for the case with tip gap and without tip gap:

Table 5.8: Performances of the initial design point and the optimum point with and without tip gap for SC1.

Efficiency	**Initial***	**Optimum***
Tip Gap [%]	81.217	82.343
No Tip Gap [%]	86.183	87.158

As for the previous analysis, also now the gap between initial and optimum design in terms of efficiency is reduced when no gap is considered, even if not substantially. This shows again that the tip leakage has an effect on the performances of the two design, but it is not the driving factor. Therefore, the reason for such difference has to

be looked for in the blade passage shape.
The normalized entropy contours are presented in Figure 5.12 for optimum and initial points:

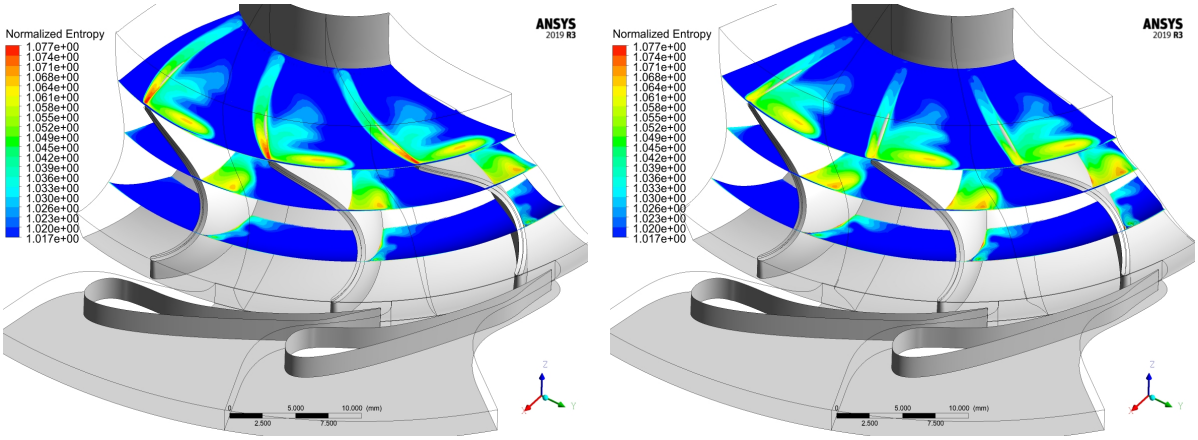

(a) Contours of normalized entropy at different meridional locations for optimum design.

(b) Contours of normalized entropy at different meridional locations for optimum design.

Figure 5.12: Contours of normalized entropy at different meridional locations for initial and optimum design.

From the images above, the presence of flow separation in both designs is evident, without big differences from an entropy generation point of view in that area, similarly to what was presented for the maximum deformation design. This suggests that the gains in efficiency are not due to a reduction of flow recirculation in this case. However, what is more interesting is the strong difference in terms of entropy generation at the trailing edge of the blade, particularly at the tip. In order to better investigate this, normalized entropy contours for different span locations, 0.2, 0.5 and 0.8 normalized span, are shown in Figure 5.13, Figure 5.14 and Figure 5.15 respectively. What can be observed from these contours is that the recirculation region is barely changed between the initial and the optimum design, confirming what just shown from the above contour. However, the main differences between initial and final design are at the leading edge and trailing edge of the blade. Although what said previously on the small influence of β_1 for many combinations of design variables still stands, it is seen how for the optimal design, the inlet angle have quite some effects on the final turbine efficiency. The following contours also confirms what just said on the higher losses due to the wake at the blade leading edge tip. In fact, the bigger and stronger region of entropy generation for the initial design at the trailing edge is evident in all the span contours.

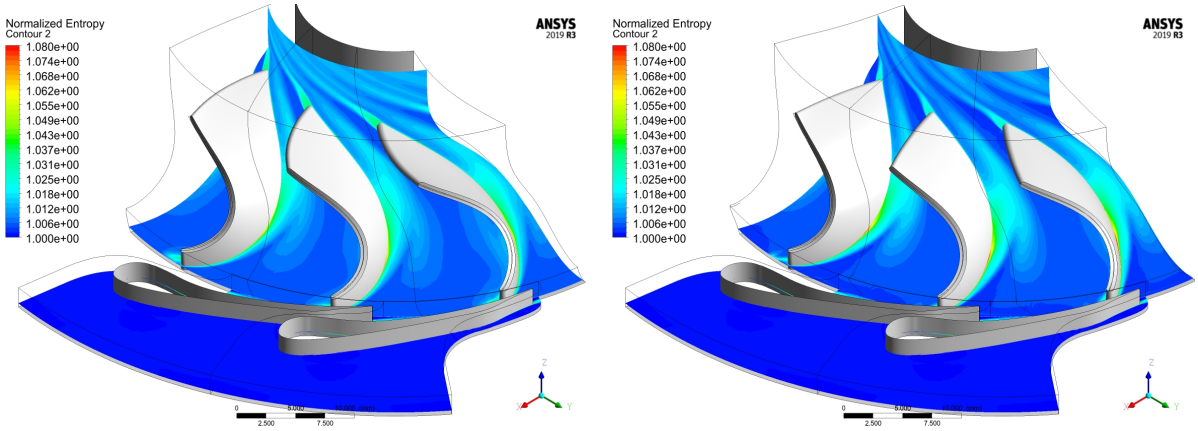

(a) Contours of normalized entropy at 0.2 span for initial design.

(b) Contours of normalized entropy at 0.2 span for optimum design.

Figure 5.13: Contours of normalized entropy at 0.2 span for initial and optimum design.

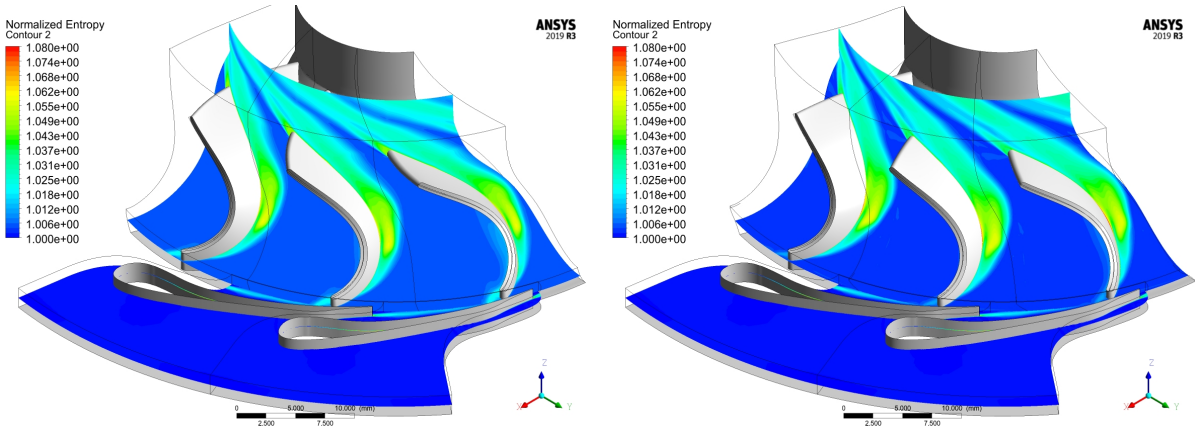

(a) Contours of normalized entropy at 0.5 span for initial design.

(b) Contours of normalized entropy at 0.5 span for optimum design.

Figure 5.14: Contours of normalized entropy at 0.5 span for initial and optimum design.

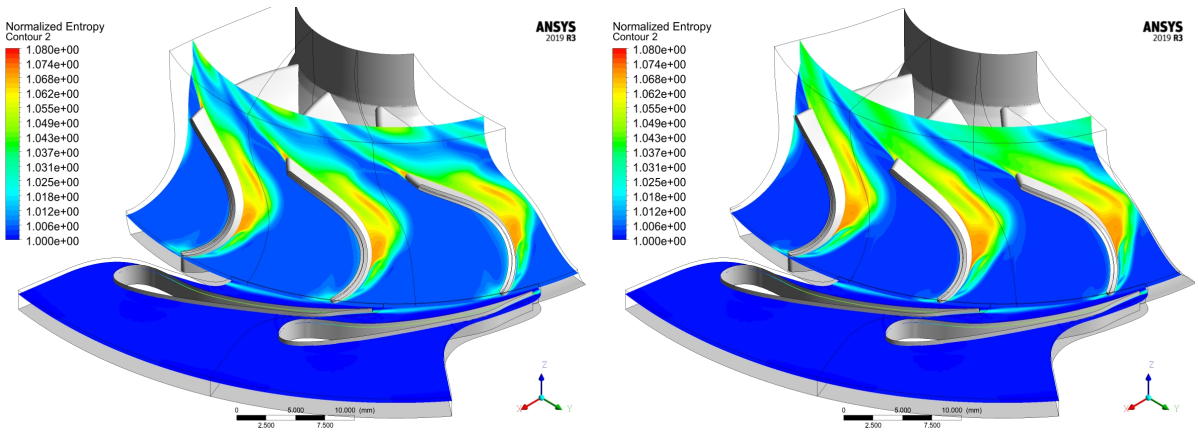

(a) Contours of normalized entropy at 0.8 span for initial design.

(b) Contours of normalized entropy at 0.8 span for optimum design.

Figure 5.15: Contours of normalized entropy at 0.8 span for initial and optimum design.

When looking at the local sensitivities for the outlet and inlet angles, shown in Figure 5.16 and Figure 5.17 respectively, it is observed that the optimum for outlet angle is well defined and found in the variable range.

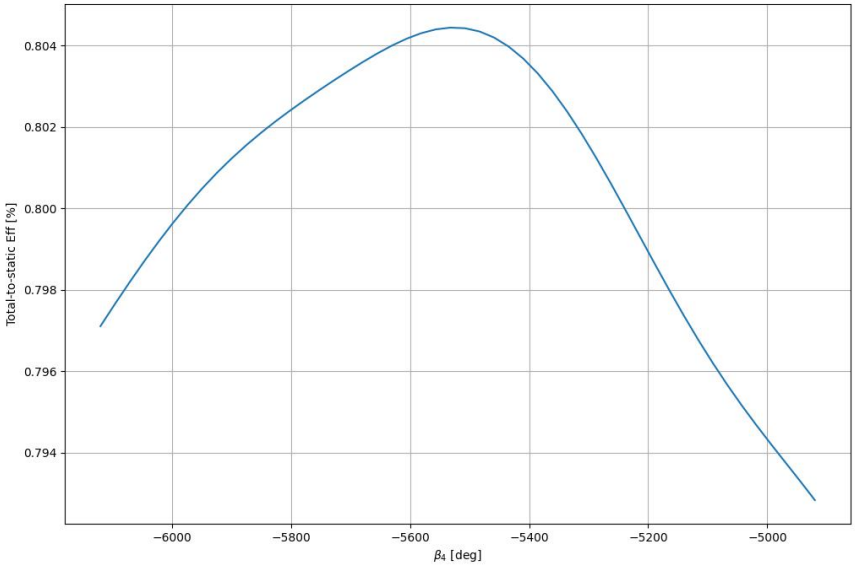

Figure 5.16: Local sensitivity of β_4 at optimum design point.

On the other hand, the range of the inlet angle seems to restrict the search for an optimum point. This suggest for an enlarging of the inlet angle range, that has however not been performed due to time constraints and will be left for future developments.

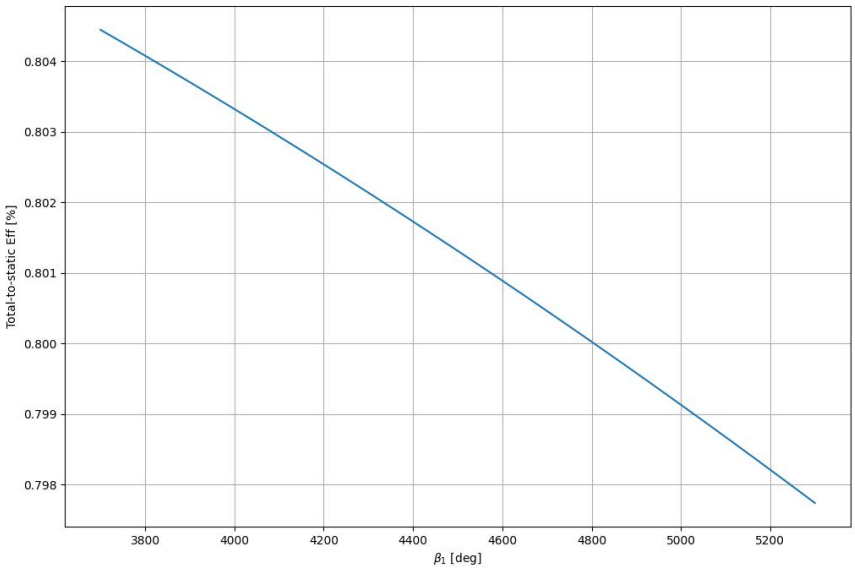

Figure 5.17: Local sensitivity of β_1 at optimum design point.

After detailed study, it is found that this flow behaviour can be explained with the concept of optimal incidence. When designing radial inlet turbines, but more generally radial turbomachines, it is found that the flow angle at the inlet of the rotating blade differs from the blade angle at the leading edge. This difference is mainly due to Coriolis forces, typical of flows in rotating reference frames. From [37] and [38], it is found that the optimal incidence for radial blades is generally increasing in absolute value when decreasing number of blades. Although similar rules of thumb were not found for backswept blades, assuming a similar behaviour as for purely radial blade, the difference in β_1 can be explained. In fact, when decreasing the value of blade inlet angle, the difference between the flow at the inlet and the blade increases, in turns enlarging the discrepancy between the two angles. Although this concept was already known when setting up the design space, its influence was apparently underestimated. To better inspect the wake and the loss generation mechanism at the blade outlet, also contours of Mach number at mid span are presented in Figure 5.18. As expected, it is clearly visible that the wake at the trailing edge is stronger for the initial design compared to the optimum point. Moreover, higher Mach numbers can be observed at the blade passage exit, and hence a stronger shock spanning from the trailing edge until the left next blade. This, together with the considerations mentioned previously explain the higher entropy at the rotor outlet for the initial design.

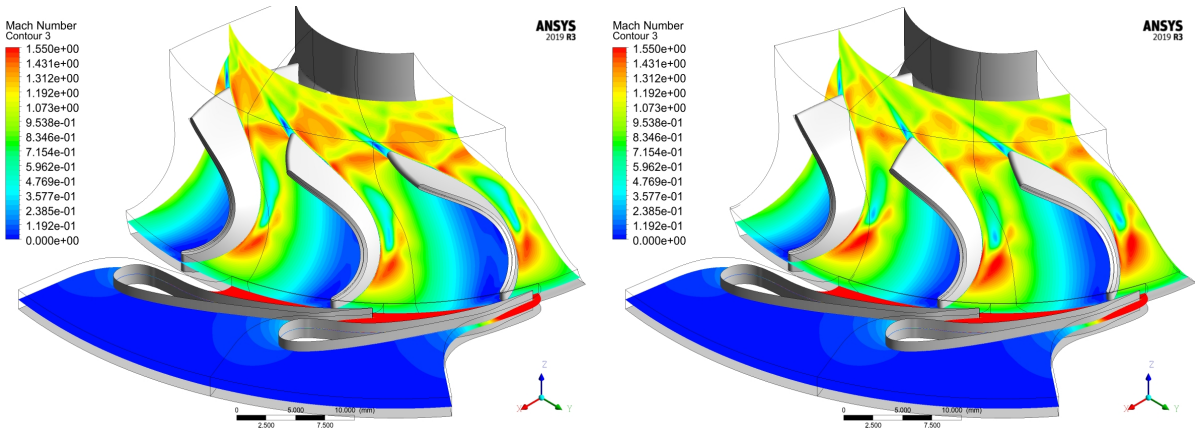

(a) Mach contours at midspan for the initial design.

(b) Mach contours at midspan for optimum design.

Figure 5.18: Mach contours at midspan for the initial and optimum design.

To have a better idea of the magnitude of difference between Mach numbers, in Table 5.9 the mass flow averaged values of relative Mach numbers for different spans are shown. What can be observed is that the hot initial design features a higher flow velocity in every span region. However, at the tip is where the most variations can be appreciated, with a mass flow averaged Mach around 0.15 higher than the optimal case.

Table 5.9: Mach number averaged at the outlet for different span regions for hot and cold design of the optimum and initial points of SC1.

Normalized Span	**Initial**	**Initial***	**Optimum**	**Optimum***
0% - 33%	0.974	0.977	0.930	0.929
33% - 66% span	1.098	1.101	1.038	1.037
66% - 100%	1.162	1.163	1.021	1.021

Moreover, in the table above the Mach number at different normalized span regions are shown also for the corresponding cold designs. As can be seen, whilst the initial design features a general increase of flow velocity at the outlet from cold to hot design, for the optimum point this trend is inverted. This difference is very limited due to the deformations in these two points being particularly small. However, this further corroborates what was said in subsection 5.1.2. In fact, it can be concluded that the initial design, deforming in the direction shown in Figure 5.2a, has a hot design where Mach numbers at the turbine trailing edge are higher due to the channel area being reduced by the deformations, and in turn reducing the total-to-static efficiency. On the other hand, the optimum point features a deformed design with higher efficiency. Looking at Table 5.9 we can already foresee that the optimum point deforms in a similar way as of Figure 5.2b, due to the Mach numbers being lower for the hot geometry. As shown in Figure 5.19, this is correct, further validating the theory of reduction and increase of passage area at the trailing edge for the different deformation behaviours, and its effect on the turbine performances.

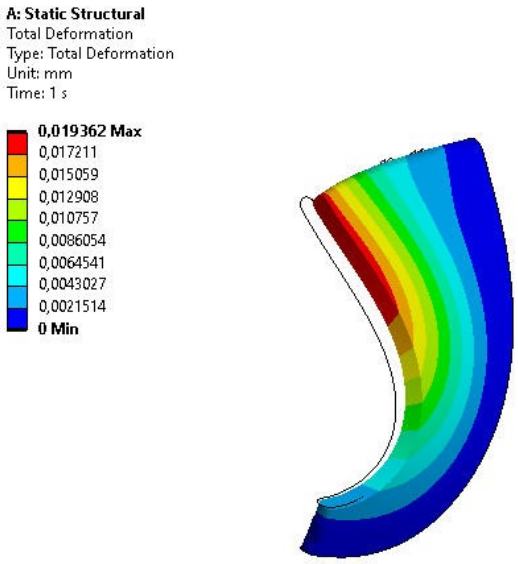

Figure 5.19: Deformation between hot and cold design for the optimum point of SC1.

From what was shown in this section, it can be concluded that an optimum is found for the investigated design space, even if the entropy generation mechanisms between initial and optimal geometry do not differ substantially. Therefore, the main motivation behind the efficiency gap between the initial design and the optimum found is attributed to the important change in outlet Mach number. In fact, this is expected to strongly influence the static quantities at the outlet, and in turns the total-to-static efficiency, objective function of the current optimization.

6

Conclusion

This last chapter summarizes all the findings found in the current research project. First of all, in section 6.1, the research questions presented in section 1.2 are reiterated and an answer based on the results shown is given for each of them. Subsequently, the main shortcomings found during the implementation and the results analysis are described in section 6.3, as well as future outlooks. Finally, in chapter 6, conclusions of the present thesis are presented.

6.1. Answers to Research Questions

Below, the research questions already shown at the beginning of the document:

Q 1 What is the maximum efficiency attainable for the 10kW Radial Inlet Turbine under study when considering manufacturing constraints?

- **Q 1.1** How much is the impact of steady elastic deformation on aerodynamic efficiency?
- **Q 1.2** What are the main differences in terms final geometry when structural deformations are considered in the design process?
- **Q 1.3** How much additional computational time is needed when structural transformation is included in the design process?

Q 2 What are the consequences resulting from the implementation of the proposed design method on the trade-off between aerodynamic efficiency and technical feasibility?

- **Q 2.1** How do the results obtained affect the decision on the most suitable manufacturing method for the turbine under study?
- **Q 2.2** What are the circumstances in which the proposed method provides the best advantages?

From the implementation of the methodology proposed and the analysis of the results, the following answers can be given:

A 1 The maximum efficiency found for the study cases studied by implementing the described optimization framework is 82.440%. This holds for the case considering additive manufacturing as production method.

A 1.1 The impact of steady elastic deformations on aerodynamic efficiency varies greatly over the design space. In particular, the maximum influence registered is found for the design point with maximum deformation for SC1, where the structural transformation resulted in an efficiency variation of the 0.79%.

A 1.2 The optimum point is found in a region of the design space where small deformations are registered and the overhang constraint is fulfilled. Therefore, the implementation of the structural transformation does not lead to substantial changes in blade geometry in this case.

A 1.3 For the test case studied in this research, the increase in computational time registered was around one third of the whole computational time. This is not a negligible increase of time resources.

A 2 The best production method resulting from the trade-off is found to be the case SC1. Therefore, manufacturing using CNC milling and stainless steel as material. This was mainly due to its advantages in terms of procurement easiness and lead time.

A 2.1 For the current study case, the optimizations have shown a small efficiency gap between the different optimum points found. This in turn resulted in a low weight of the efficiency in the decision of the best production method and material to be used.

A 2.2 Keeping in mind that this optimization framework is mostly useful for highly loaded turbomachines, it can be said that the developed method is mainly advantageous when the best efficiency point is subject to strong deformations, or the theoretical optimum falls in a constrained area of the design space. In fact, these are the situations where the efficiency would vary the most, compared to a CFD-based optimization. However, the location of the optimum is not known beforehand, adding credit to the developed method.

6.2. Shortcomings and Future Outlooks

A list of shortcomings for the current optimization framework is presented below:

- The multidisciplinary optimization implemented resulted to be around 33% more computationally expensive compared to its CFD-based counterpart. This made the process quite lengthy, and led to the decision of reducing the number of design variables, together with other measures to reduce the simulation time.
- The method applied to SC3, resulted in the failure of some of the design points chosen by the Design of Experiment algorithm. Although the design points that failed to computed were automatically replaced, this might lead to less uniform

spread of training points, in turn reducing the response surface accuracy. For this case, the accuracy of SC3 was still found acceptable, but in general this shows a lack of robustness in the optimization for that specific study case

- The implementation of fillets in the analysis of the blade is currently not supported by the optimization framework. This is deemed an important shortcoming of the current method, since the analysis of equivalent stresses during the optimizations would allow the avoidance of possible design iterations due to the parts not being structurally viable. Moreover, the addition of this information would allow for the implementation of important constraints on the safety factor of the part, especially if combined with the implementation of blade thickness distribution in the optimization.
- As shown in Figure 5.17, the width of the range provided to the inlet angle design variable seems not to be sufficient. In fact, it is shown from the local sensitivity of this variable at the optimum design, that an further decrease of such variable would have been beneficial for the turbine performances.

Once the main shortcomings have been presented, possible solutions for each of them have been considered. These can be found below:

- The system coupling module in Ansys Workbench does not currently allow to specify different convergence requirement for different coupling iterations. This limitation leads to a significant increase of computational time. This would allow to perform the first steps of the coupling with a reduced number of CFD iterations, just to have a gradual change in blade shape and avoid numerical errors. On the other hand, the number of iterations for the last coupling step would still have to remain high enough to ensure full convergence of the CFD simulation, and hence accurate prediction of the blade final shape.
  Moreover, a study on the influence of pressure loads on the efficiency gap between hot and cold design is deemed important. In fact, if the pressure loads were found to have a negligible influence on turbine efficiency, this would allow for the use of a 1-way coupling simulation, further reducing computational time.
- In order to increase the coupling robustness, the number of coupling iterations can be increased. This would however only be possible if the previous point was satisfied, because otherwise the computational time would be rise excessively.
  Moreover, an increase in mesh size in correspondence of the blade surface would strongly reduce the appearance of negative mesh elements due to mesh displacement. This would also result in lower computational time, although reducing the accuracy of the simulations. The use of a different turbulence model rather than SST might be investigated for future applications, since methods like $k - \epsilon$ are known to require for far less wall mesh refinement.
- The inclusion of fillets should be possible in Ansys Workbench, for all the used modules. However, this would require the addition of the hub in the structural simulations leading to a steep increase of mesh size in the solid domain, and probably a less robust generation of fluid dynamic numerical grid due to the fillet modelling. Therefore, this would lead to a general increase of computational time.

- For this specific case, an increase in the range of β_1 would be beneficial in terms of turbine efficiency.

6.3. General Overview and Main Conclusions

As mentioned in previous chapters, the current research project aims at creating a multidisciplinary optimization framework, which allows to consider manufacturing constraints and deformations already at an early phase of the design phase. This has been achieved by using the cold geometry as initial guess, and by performing steady state 2-way fluid-structure interaction simulations at each design point of a surrogate-based optimization. The test case used is a mini radial inlet turbine for ORC applications to be implemented in the ORCHID test facility.
The optimization has been performed on three different study cases featuring different manufacturing methods and materials:

- SC1: part in stainless steel produced by CNC milling;
- SC2: part in titanium produced by CNC milling;
- SC3: part in stainless steel produced by additive manufacturing;

By means of this framework, the behaviour of the structure and the flow field, and their interaction have been investigated by changing the rotor blade angles and curvature, at hub and tip respectively.
A total of 68 fsi simulations have been performed, leading to around 3 days of computational time for each study case. The design of experiment algorithm used was the Optimal Space Filling, whilst Kringing and NLPQL have been used for the response surface generation and the research of the optimal point respectively.

The results showed that the main contribution to the structural deformations of the part comes from the centrifugal loads for each case. Meaning that the pressure load contribution might have been neglected, reducing in this way the computational effort. However, this needs to be investigated further, since there might be areas of the design space where the deformations due to pressure loads are more preeminent. Moreover, it has been observed that the blade undergoes different deformation behaviour over the design space. This is particularly interesting for the sizing of the tip gap of the part.
To further corroborate the importance of a multidisciplinary study, it has been shown that for the study case investigated, the deformations can be as high as 0.461mm at the blade leading edge tip. Due to this, a difference of 0.64% efficiency has been registered between hot and cold design, which is particularly high considered the reduced design space, where efficiency varies of around 4% at most.
The best total-to-static efficiency registered, is for the SC3 with a value of 82.44%. However, the manufacturing method chosen from the trade-off performed has been CNC milling, which features an optimum efficiency of 82.343%, around 1.13 percentage points higher than the initial guess. This increase in efficiency was mainly driven by reduction of entropy generation at the inlet of the blade, due to an incidence angle closer to the optimal value, and at the trailing edge due to a more expanded, and

hence slower relative flow in that region,leading to a smaller wake and lower shock losses.

Generally speaking, it can be said that the multidisciplinary framework proposed have the advantages of providing additional information regarding the structural behaviour of the part, compared to a normal CFD-based optimization. Moreover, the implementation of such method would be mainly beneficial if the optimum was found in a region of high deformations, or on a constrained area of the design space, which is not the case for the ORCHID turbine rotor.
For future developments of the method, it is suggested to look into the implementation of fillets to also asses the behaviour of stresses over the design space, the investigation of way to reduce the currently elevated computational effort, and to increase robustness of the coupling, by either increasing the coupling iterations, or reducing the mesh refinement.

References

[1] L. Mueller, Z. Alsalihi, and T. Verstraete. “Multidisciplinary optimization of a turbocharger radial turbine”. In: *Journal of Turbomachinery* (2013). DOI: 10.1115/1.4007507.

[2] J. Peter and M. Marcelet. “Comparison of surrogate models for turbomachinery design”. In: *WSEAS Transactions on Fluid Mechanics* (Jan. 2008).

[3] Zhihui Li and Xinqian Zheng. “Review of design optimization methods for turbomachinery aerodynamics”. In: *Progress in Aerospace Sciences* (2017). DOI: 10.1016/j.paerosci.2017.05.003.

[4] S. Koziel and X. Yang. *Computational optimization, methods and algorithms*. Springer, 2011.

[5] J. R. R. A. Martins and A. Ning. *Engineering Design Optimization*. Cambridge University Press, 2021. DOI: 10.1017/9781108980647.

[6] A. Forrester and A. J. Keane. “Recent advances in surrogate-based optimization”. In: *Progress in aerospace sciences* (2009). DOI: 10.1016/j.paerosci.2008.11.001.

[7] A. R. Collar. “The Expanding Domain of Aeroelasticity”. In: *The Journal of the Royal Aeronautical Society* (1946). DOI: 10.1017/S0368393100120358.

[8] T. Verstraete, Z. Alsalihi, and R. A. Van den Braembussche. “Multidisciplinary Optimization of a Radial Compressor for Micro Gas Turbine Applications”. In: Turbo Expo: Power for Land, Sea, and Air Volume 6: Turbo Expo 2007, Parts A and B (May 2007). DOI: 10.1115/GT2007-27484.

[9] J.G. Marshall and M. Imregun. “A review of aeroelasticity methods with emphasis on turbomachinery applications”. In: *Journal of fluids and structures* (1996). DOI: 10.1006/jfls.1996.0015.

[10] H. Yang et al. “Comparative analysis of numerical methods for rotor blade unrunning design”. In: *6th International Symposium on Fluid Machinery and Fluid Engineering*. 2014. DOI: 10.1049/cp.2014.1221.

[11] G. Saiz. “Turbomachinery aeroelasticity using a time-linearised multi blade-row approach”. PhD thesis. 2008.

[12] C. M. De Servi et al. “Design Method and Performance Prediction for Radial-Inflow Turbines of High-Temperature Mini-Organic Rankine Cycle Power Systems”. In: *Journal of Engineering for Gas Turbines and Power* (2019). DOI: 10.1115/1.4043973.

[13] A. J. Head et al. “Preliminary Design of the ORCHID: A Facility for Studying Non-Ideal Compressible Fluid Dynamics and Testing ORC Expanders”. In: Turbo Expo: Power for Land, Sea, and Air. 2016. DOI: 10.1115/GT2016-56103.

[14] E. Oñate. *Structural analysis with the finite element method. Linear statics, volume 2*. Springer Science & Business Media, 2013. DOI: 10.1007/978-1-4020-8743-1.

[15] N. Perez. *Linear Elastic Fracture Mechanics*. Springer, 2004. DOI: 10.1007/978-3-319-24999-5.

[16] *Mechanical APDL Theory Reference*. ANSYS Inc., 2013.

[17] J. Guerrero. "Introduction to Computational Fluid Dynamics: Governing Equations, Turbulence Modeling Introduction and Finite Volume Discretization Basics." In: (2015).

[18] *Modeling tecniques for fluid machines*. Lecture Slides, Politecnico di Milano.

[19] J. H. Ferziger and M. Perić. *Turbulent Flows*. Springer Berlin Heidelberg, 2002. DOI: 10.1007/978-3-319-99693-6_10.

[20] W.P. Jones and B.E. Launder. "The prediction of laminarization with a two-equation model of turbulence". In: *International Journal of Heat and Mass Transfer* (1972). DOI: 10.1016/0017-9310(72)90076-2.

[21] D. C. Wilcox et al. *Turbulence modeling for CFD*. Vol. 2. DCW industries, 1998. URL: https://books.google.it/books?id=VwlRAAAAMAAJ.

[22] F. R. Menter. "Zonal two equation kw turbulence models for aerodynamic flows". In: *23rd fluid dynamics, plasmadynamics, and lasers conference*. 1993. DOI: 10.2514/6.1993-2906.

[23] F. R. Menter. "Two-equation eddy-viscosity turbulence models for engineering applications". In: *AIAA journal* (1994). DOI: 10.2514/3.12149.

[24] G. Hou, J. Wang, and A. Layton. "Numerical Methods for Fluid-Structure Interaction. A Review". In: *Communications in Computational Physics* (2012). DOI: 10.4208/cicp.291210.290411s.

[25] F. Benra et al. "A comparison of one-way and two-way coupling methods for numerical analysis of fluid-structure interactions". In: *Journal of applied mathematics* (2011). DOI: 10.1155/2011/853560.

[26] *System Coupling User's Guide*. ANSYS Inc., 2013.

[27] *Design Exploration User's Guide*. ANSYS Inc., 2013.

[28] E. Andrés-Pérez et al. *Evolutionary and deterministic methods for design optimization and control with applications to industrial and societal problems*. Springer, 2018. DOI: 10.1007/978-3-319-89890-2.

[29] K. Schittkowski. "NLPQL: A FORTRAN subroutine solving constrained nonlinear programming problems". In: *Annals of operations research* (1986). DOI: 10.1007/BF02022087.

[30] K. Schittkowski. "On the convergence of a sequential quadratic programming method with an augmented lagrangian line search function". In: *Mathematische Operationsforschung und Statistik. Series Optimization* (1983). DOI: 10.1080/02331938308842847.

[31] R.S. Oliveira. “Assessment and impact of aeroelastic effects in highly supersonic organic Rankine cycle turbines”. In: (2020). DOI: 10.1115/1.4033973.

[32] Nickel Development Institute. “High-temperature characteristics of stainless steel”. In: *A designer’s handbook series N.9004*. 2014.

[33] S. Kumar, K. Chattopadhyay, and V. Singh. “Tensile behavior of Ti-6Al-4V alloy at elevated temperatures”. In: *Proceeding the international conference on multifunctional materials, structure and applications*. 2014.

[34] C. Rodgers and R. Geiser. “Performance of a High-Efficiency Radial/Axial Turbine”. In: *Journal of Turbomachinery* 109.2 (Apr. 1987), pp. 151–154. DOI: 10.1115/1.3262077.

[35] A.C. Jones. “Design and Test of a Small, High Pressure Ratio Radial Turbine”. In: Turbo Expo: Power for Land, Sea, and Air Volume 1: Turbomachinery (June 1994). DOI: 10.1115/94-GT-135.

[36] A. C. Jones. “Design and Test of a Small, High Pressure Ratio Radial Turbine”. In: *Journal of Turbomachinery* 118.2 (Apr. 1996), pp. 362–370. DOI: 10.1115/1.2836651.

[37] A.J. Glassman. *Turbine design and application*. 1972.

[38] A. Whitfield. “Slip Factor of a Centrifugal Compressor and Its Variation with Flow Rate”. In: *Proceedings of the Institution of Mechanical Engineers* (1974). DOI: 10.1243/PIME_PROC_1974_188_047_02.